

## Interconnected assembly factors regulate the biogenesis of mitoribosomal large subunit

Victor Tobiasson<sup>1†</sup>, Ondřej Gahura<sup>2†</sup>, Shintaro Aibara<sup>1,4†</sup>, Rozbeh Baradaran<sup>1</sup>, Alena Zíková<sup>2,3\*</sup>, Alexey Amunts<sup>1\*</sup>

<sup>1</sup> Science for Life Laboratory, Department of Biochemistry and Biophysics, Stockholm University, 17165 Solna, Sweden.

<sup>2</sup> Institute of Parasitology, Biology Centre, Czech Academy of Sciences, Ceske Budejovice, Czech Republic

<sup>3</sup> Faculty of Science, University of South Bohemia, Ceske Budejovice, Czech Republic.

<sup>4</sup> Current address: Department of Molecular Biology, Max-Planck-Institute for Biophysical Chemistry, Göttingen, Germany.

† The authors contributed equally to this work.

\* correspondence to: amunts@scilifelab.se, azikova@paru.cas.cz

## Abstract

Mitoribosomes consist of ribosomal RNA and protein components, coordinated assembly of which is critical for function. We used mitoribosomes with reduced RNA and increased protein mass from *Trypanosoma brucei*, to provide insights into the biogenesis of mitoribosomal large subunit. Structural characterisation of a stable assembly intermediate revealed 22 assembly factors, some of which are also encoded in mammalian genomes. The assembly factors form a protein network that spans over 180 Å, shielding the ribosomal RNA surface. The entire central protuberance and L7/L12 stalk are not assembled, and require removal of the factors and remodeling of the mitoribosomal proteins to become functional. The conserved proteins GTPBP7 and mt-EngA are bound together at the subunit interface in proximity to the peptidyl transferase center. A mitochondrial acyl-carrier protein plays a role in docking the L1 stalk which needs to be repositioned during maturation. Additional enzymatically deactivated factors scaffold the assembly, while the exit tunnel is blocked. Together, the extensive network of the factors stabilizes the immature sites and connects the functionally important regions of the mitoribosomal large subunit.

36 **Introduction**

37 Mitoribosomes differ from bacterial and cytosolic ribosomes in their ribosomal RNA (rRNA),  
38 protein content, overall size, and structure. Their formation is an intricate and hierarchical pro-  
39 cess involving multiple proteins and RNA molecules working in coordination and under tight  
40 regulation (Pearce et al 2017). The cooperative effort involves regulation of two genomes, be-  
41 cause rRNA is encoded by the organellar genome, and almost all the mitoribosomal proteins and  
42 assembly factors are encoded by the nuclear genome and therefore imported from the cytosol  
43 (Couvillion et al 2016). Finally, the fundamental process of the mitoribosomal assembly is com-  
44 plicated due to the localization of its large subunit (mtLSU) to the inner mitochondrial mem-  
45 brane. Therefore, stages of assembly were suggested to involve specific steps and kinetics (Bo-  
46 genhagen et al 2014; Antonicka and Shoubridge 2015; De Silva et al 2015). The presence of dif-  
47 ferent compositions is hypothesized to promote formation of defined pre-mitoribosomal com-  
48 plexes with as-yet-unknown organelle-specific auxiliary factors.

49 Mitochondria of *Trypanosoma brucei* provide a good model for studying the assembly process,  
50 because their mitoribosomes consist of over a hundred components, and the ratio of protein to  
51 rRNA is unusually high (Zikova et al 2008; Ramrath et al 2018). Since the rRNA forms a com-  
52 pact core of the mitoribosome, and proteins are mostly peripherally associated, an architecture  
53 based on the reduced rRNA and supernumerary mitoribosomal proteins would need additional  
54 stabilization for its assembly. Therefore, it increases the chances to characterize defined pre-mi-  
55 toribosomal complexes, which are not stable enough for biochemical isolation in mitochondria of  
56 other species. Indeed, structural characterization of an assembly intermediate of the *T. brucei* mi-  
57 toribosomal small subunit (mtSSU) provided insight into its assembly pathway with many newly  
58 detected proteins (Saurer et al 2019).

59 The mtLSU accommodates the peptidyl transferase center (PTC) that catalyzes formation of pep-  
60 tide bonds between amino acids, tRNA binding sites, the L7/L12 stalk that is responsible for the  
61 recruitment of translation factors, the L1 stalk, the central protuberance (CP) that facilitates com-  
62 munication between various functional sites, and the exit tunnel to egress a synthesized protein.  
63 In bacteria, our understanding of the LSU assembly is relatively limited (Davis and Williamson  
64 2017). It comes primarily from a characterization of the final maturation stages (Li et al 2013;  
65 Jomaa et al 2014; Ni et al 2016), studies on incomplete LSU particles as a result of protein deple-  
66 tion (Davis et al 2016), as well as *in vitro* reconstitution studies with purified ribosomal RNA  
67 and protein components (Nikolay et al 2018). These studies identified different LSU precursors  
68 with assembly factors bound to rRNA components (Davis and Williamson 2017). In mitochon-  
69 dria, the mtLSU lacks many of the rRNA components involved in the canonical pathways, and  
70 higher complexity of the interactions between the mitoribosomal proteins at the functional sites  
71 has evolved (Ott et al 2016; Greber and Ban 2016). A functional mtLSU requires a folded rRNA  
72 core, a flexible L1 stalk that is involved in tRNA movement, an extended L7/L12 protrusion for  
73 binding of translational factors, and a proteinaceous CP formed by mitochondria-specific ele-  
74 ments involved in tRNA binding (Aibara et al 2020; Tobiasson and Amunts 2020). However,  
75 only the final stage of the mtLSU assembly with fully mature functional sites has been visualized

76 (Brown et al 2017; Itoh et al 2020), and no preceding steps in the formation have been detected.  
77 Therefore, mtLSU assembly remains poorly understood.

78 To provide insight into the process of the mtLSU assembly, we determined the cryo-EM struc-  
79 ture of a native *T. brucei* mtLSU assembly intermediate (pre-mtLSU) in a complex with assem-  
80 bly factors. Most of the assembly factors have not been previously implicated in mitoribosomal  
81 biogenesis. The structural data suggests that the biogenesis relies on an extensive protein net-  
82 work formed by the assembly factors that connect a premature PTC, the L1 and L7/L12 stalks  
83 with the CP, while the exit tunnel is blocked. A homology search suggests that some of the  
84 newly identified assembly factors are also conserved in mitochondria from other species, includ-  
85 ing mammals, and therefore may represent general principles. Comparison with two bacterial as-  
86 sembly intermediates (Zhang et al 2014; Seffouh et al 2019) further provides insights into the  
87 conserved GTPases GTPBP7 and mt-EngA bound at the subunit interface.

88

## 89 **Results**

### 90 **Structural determination and composition of the native pre-mtLSU complex**

91 We used a *T. brucei* procyclic strain grown in low-glucose medium that maintains translationally  
92 active mitochondria. Mitoribosomal complexes were purified directly from *T. brucei* mitochon-  
93 dria and analyzed by single-particle cryo-EM. During image processing, in addition to the intact  
94 monosomes, we detected a pool of free subunits. We focused the analysis on this population and  
95 through 3D classification isolated a homogeneous subset of pre-mtLSUs that corresponded to  
96 ~3.5 % of the particles combined from five data sets.

97 896,263 particles were picked using Warp (Tegunov and Cramer 2019), and further processed  
98 using RELION (Kimanis et al 2016; Zivanov et al 2018). We performed reference-based 3D  
99 classification with references generated from a preliminary classification of a screening data set.  
100 This resulted in 207,788 particles corresponding to the mtLSU shape but distinct from that of a  
101 mature mtLSU of which we found 152,816 particles. Refinement of those assigned and subse-  
102 quent classification using fine-angular searches with a solvent mask identified 32,339 pre-  
103 mtLSU particles (Appendix Fig S1). To improve the angles further, the particles were subjected  
104 to masked auto-refinement. Following the CTF refinement, we obtained a reconstruction of a  
105 pre-mtLSU that likely reflects a stable premature complex. This was evidenced by the presence  
106 of densities corresponding to conserved ribosomal assembly factors.

107 The cryo-EM reconstruction was refined to 3.50 Å resolution (Table S1). This allowed us to  
108 build a ~2.2 MDa model and assign assembly factors, as well as additional mitoribosomal pro-  
109 teins, directly from the density (Figs 1 and 2, Appendix S2). Six distinct features define the over-  
110 all pre-mtLSU; 1) the rRNA domain V is well resolved and covered by newly identified mito-  
111 chondria-specific assembly factors, 2) the subunit interface consists almost entirely of newly  
112 identified assembly factors and two conserved GTPases, 3) the proteinaceous CP is absent, 4) the  
113 L7/L12 stalk proteins are missing, and its rRNA platform is not folded, instead assembly factors

114 occupy similar positions, 5) the L1 stalk is shifted inward ~30 Å and linked to the CP base by as-  
115 sembly factors, and 6) the exit tunnel is blocked. Due to these features, compositional and con-  
116 formational changes are required for the maturation of the pre-mtLSU. In terms of the mitoribo-  
117 somal proteins, 18 previously identified proteins are missing from the structure of the pre-  
118 mtLSU. Seven of these have bacterial homologs (uL10m, uL12m, uL16m, bL27m, bL31m,  
119 bL33m and bL36m) and the rest are mitochondria specific (Fig 1, Table S2). Additionally, we  
120 assigned sequences to previously unidentified mtLSU proteins uL14m and mL101 (Fig 2).

121 Following the previously identified mitoribosomal small subunit assembly factors (Saurer et al  
122 2019), we adopt a similar nomenclature for the mitochondria specific large subunit factors.  
123 Therefore, we refer to them as mitochondrial Large subunit Assembly Factor(s) (mt-LAF). Proteins with mitochondrial homologs are referred to as their human names. Proteins with bacterial  
124 homologs but not identified in humans are referred to as their bacterial names with the prefix  
125 “mt-“. The identified assembly factors of the mitoribosome include two homologs of bacterial  
126 GTPase assembly factors GTPBP7 (RbgA in bacteria) and mt-EngA, a homolog of the ribosome  
127 silencing factor mt-RsfS (MALSU1), a DEAD-box RNA helicase (mt-LAF2), two pseudouridine-  
128 dinases, RPUSD4 and mt-LAF4, as well as a methyltransferase MRM, two copies of the mito-  
129 chondrial acyl-carrier protein mt-ACP, two LYR-motif-containing proteins L0R8F8 and mt-  
130 LAF18. Finally, six other proteins with previously unassigned functions mt-LAF7, 8, 12, 14, 15,  
131 19 are present. In the model, we included only the parts for which backbone geometry is appar-  
132 ent. Other regions with only partial or poor density visible were modeled as UNK1-11.

134

### 135 **GTPase mt-RbgA (GTPBP7) is structurally linked to the mitoribosomal core via specific 136 assembly linkers**

137 We started the structural analysis by searching for similar assembly intermediate architectures in  
138 bacterial counterparts. Particles with an absent CP were reported previously in RbgA-depleted  
139 *Bacillus subtilis* cells. RbgA was then added *in vitro* and shown to bind to the complex, which  
140 identified its role as an assembly factor (Seffouh et al 2019). RbgA belongs to the Ras GTPase  
141 family typically containing a low intrinsic GTPase activity which is increased in the presence of  
142 a mature LSU subunit (Achila et al 2012). It has an N-terminal GTPase domain and a C-terminal  
143 helical domain that forms a five-helix bundle (Pausch et al 2018). In the pre-mtLSU structure,  
144 we found a conserved mitochondrial homolog of RbgA, GTPBP7. Studies in yeasts reported that  
145 deletion of this protein (Mtg1 in yeast) results in respiration deficiency (Barrientos et al 2003).  
146 In *B. subtilis*, where this assembly factor is essential, the LSU:RbgA complex showed that the N-  
147 terminal domain overlaps with rRNA H69 and H71, and that the C-terminal helical domain inter-  
148 acts with H62 and H64 (Seffouh et al 2019). In this position, RbgA displaces the P-site and fur-  
149 ther interacts with the surrounding rRNA, including H92 and H93. Therefore, the binding of  
150 RbgA requires specific contacts with rRNA. In our map of the *T. brucei* pre-mtLSU, the corre-  
151 sponding rRNA regions forming the binding site for GTPBP7 are not observed. However, the  
152 comparison of our structure with the *B. subtilis* LSU:RbgA complex (PDB ID 6PPK) shows

153 nearly identical conformation of the factor on the pre-*mtLSU* complex (Fig EV1). This includes  
154 the peripheral interaction between the GTPBP7 C-terminal domain and the mitoribosomal pro-  
155 tein uL14m (Fig 3). In addition, the position of the catalytic GTPase site is also conserved, alt-  
156 though the nucleotide binding site of GTPBP7 is empty (Fig 3B). A mutational analysis previ-  
157 ously identified His67 (His9 in *B. subtilis*) as a key catalytic residue, and its correct confor-  
158 mation is guided by rRNA (Gulati et al 2013). Despite the overall conservation in mitochondria,  
159 the rRNA that is proposed to position the residue in bacteria is missing in our pre-*mtLSU* struc-  
160 ture.

161 We found that the conserved position of GTPBP7 in *T. brucei* is maintained through two special-  
162 ized assembly linkers (Fig 3A). The first linker is established between the C-terminal domain  
163 and the MRM N-terminal helix. The latter adopts a crescent shape around the  
164 C-terminal domain of GTPBP7, forming a series of contacts with four out of its five helices (Fig  
165 3A). The second linker is provided by RPUSD4 approaching from the mitoribosomal core. It in-  
166 teracts with the GTPBP7 C-terminal domain and contributes a  $\beta$ -strand to a shared  $\beta$ -sheet (Fig  
167 EV2B). Therefore, GTPBP7 is anchored to the flexible rRNA core via two dedicated factors that  
168 compensate for the lack of rRNA contacts.

169 RPUSD4 belongs to a family of site-specific RluD pseudouridine synthases involved in the bac-  
170 terial LSU assembly and responsible for creating of pseudouridines at positions 1911, 1915 and  
171 1917 (*E. coli* numbering) in the H69 end-loop (Gutgsell et al 2001; Gutgsell et al 2005). In our  
172 pre-*mtLSU* structure, RPUSD4 encircles the immature rRNA nucleotides A1008-C1013 as well  
173 as U1075-U1086 with the connecting nucleotides being unstructured (Figs EV2A and EV4). Its  
174 active site is occupied by cytosine C1010 of H90 forming hydrogen bond with glutamic acid  
175 E316 (Fig EV2A), suggesting lack of catalytic activity in the detected state. The N-terminal do-  
176 main of RPUSD4 is positioned at the distance of  $\sim$ 80 Å facing towards the L7/L12 stalk. Thus,  
177 *T. brucei* RPUSD4 performs a stabilizing role for GTPBP7 at the subunit interface and connects  
178 with the L7/L12 stalk to coordinate the maturation of the different functional sites (Fig 4A,B).

179 MRM belongs to the family of SpoU RNA methyltransferases, but appears to have a closed ac-  
180 tive site obstructed by Phe334, Arg327 and Glu417 that prevents the binding of the typical S-  
181 adenosyl methionine cofactor (Fig EV2B), and the sequence of the conserved motif (Hori 2017)  
182 is disrupted (Appendix Fig S3). It is located peripherally, and bound to the mitoribosome via a  
183 C-terminal 24-residue helix interacting with rRNA H41/42, and via contacts with mt-LAF12 (Fig  
184 EV2B).

185 Together, RPUSD4 and MRM/mt-LAF12 perform a structural scaffolding role for binding  
186 GTPBP7. A homology search of the assembly factors reveals that RPUSD4 and MRM are also  
187 present in most eukaryotes (Fig 4C). Since GTPBP7 is present in other organisms, our data sug-  
188 gests the reported cooperative action of the assembly factors might be conserved.

189

190 **GTPase mt-EngA is stabilized via protein extensions**

191 In the subunit interface, we identified another conserved GTPase homolog, mt-EngA. It contains  
192 two GTPase domains arranged in tandem as well as a C-terminal K homology (KH) domain  
193 which is pointed towards the PTC. We could model two GTPs in the GTPase domains (Fig 3B).  
194 The overall position of mt-EngA is identical to bacteria, suggesting functional conservation. The  
195 assembly factor occupies the space between the PTC and the E-site (Fig EV1), and a role in  
196 chaperoning rRNA has been proposed (Zhang et al 2012). However, the comparison with *E. coli*  
197 LSU:EngA complex reveals conformational differences that highlight the nature of the mito-  
198 chondrial protein-rich system, and its role in the stabilization of the conserved assembly factor.  
199 Firstly, the N-terminal GTPase domain is extended by 60 residues, with residues 101-108 stabili-  
200 lizing a helix-turn-helix motif (275-305), which remained unresolved in the bacterial complex  
201 (Fig EV1B). The N-terminal extension is generally present in mitochondria from other species  
202 (Appendix Fig S4). This motif is important for the stabilization of mt-EngA, because one helix is  
203 stacked against a helix of mt-LAF2, whereas the other forms a helical bundle with mt-LAF14  
204 (Fig EV3).  
205 Secondly, the N-terminal residues 72-75 of EngA stabilize a short helix (residues 367-374),  
206 which is buried within rRNA groove via Arg367 and Arg369 (Fig 3B). It disrupts the local struc-  
207 ture of H75 and stabilizes the flipped nucleotide A894. This loop is also highly charged in the  
208 corresponding *E. coli* structure, but does not adopt the helical conformation observed here. Fi-  
209 nally, the N-terminus forms additional contacts with five mitoribosomal proteins (bL28m,  
210 bL35m, bL19m, mL64, mL74), a stabilizing protein mass that compensates for the missing  
211 rRNA in this region. Overall, while the N-terminal GTPase domain aligns well with the bacterial  
212 EngA, its interacting partners in our structure are more proteinaceous and specific to mito-  
213 chondria.  
214 The conserved globular domains of mt-EngA are associated with the pre-mtLSU core via mt-  
215 LAF14. Its three helices from the N-terminus encloses the N-terminal GTPase domain helix 230-  
216 242 (Fig EV3). Here, mt-LAF14 replaces the missing rRNA H82-87 and protein L1, which binds  
217 the EngA N-terminal GTPase domain in bacteria. Factor mt-LAF14 spans over 100 Å to the top  
218 of the CP, where it also stabilizes unwound rRNA (Figs 4, EV4). Thus, mt-EngA is bound via a  
219 protein extension and also associated with the protein-based scaffold of assembly factors, includ-  
220 ing the high molecular weight mt-LAF2 and mt-LAF14, which are connected to the CP.

221

## 222 **The module GTPBP7:mt-EngA coordinates maturation of interfacial rRNA**

223 The process of the LSU assembly is dynamic with a cooperative action of different assembly fac-  
224 tors (Davis et al 2016; Davis and Williamson 2017). Although GTPBP7 and EngA have previ-  
225 ously been visualized separately on the bacterial LSU through deletion and reconstitution experi-  
226 ments, our cryo-EM structure shows both factors simultaneously associated with the pre-mtLSU  
227 and with each other. The presence of both factors rationalizes why rRNA domain V is better re-  
228 solved than in the mature mt-LSU (Fig 5). We were able to model 33% more nucleotides relative

229 to the mature mt-LSU, which shows that the H89-93 region does not occupy the expected bacte-  
230 rial position and highlights a need for prominent remodeling during maturation (Appendix Figs  
231 S5 and S6).

232 The contacts between GTPBP7 and mt-EngA are formed via the N-terminal domain and KH do-  
233 mains, respectively (Fig 3B). The shared surface area is ~500 Å, and each of the domains is also  
234 associated with rRNA. The contacts formed between GTPBP7 and mt-EngA include electrostatic  
235 interactions, as well as hydrophobic residues (Fig 3B). Since the structures and positions of both  
236 factors are conserved with bacteria, and we identified homologs in representative eukaryotic spe-  
237 cies, these results indicate that the simultaneous binding might be a conserved feature.

238

### 239 **DEAD-Box helicase mt-LAF2**

240 In the region connecting the CP with the body of the pre-mtLSU, a conserved ATP-dependent  
241 DEAD-box (Asp-Glu-Ala-Asp) RNA helicase was found, namely mt-LAF2. It belongs to a large  
242 family of RNA helicases that unwind short RNA duplexes and participate in different aspects of  
243 cellular processes, including cell cycle regulation, apoptosis, and the innate immune response  
244 (Xing et al 2019).

245 Factor mt-LAF2 is one of the largest mitoribosomal assembly factors (Fig 2B), spanning 110 Å  
246 through the rRNA core to the CP (Figs 4 and 6, Figure EV4). It contains two helicase domains; a  
247 DEAD-box and a Helicase C domain (helicase 1 and 2, Fig 6). The two helicases together form  
248 the conserved fold for RNA and ATP binding with a linker between them. Typical terminal ex-  
249 tensions are also present, and the extended C-terminus anchors mt-LAF2 to the rRNA core by  
250 forming contacts at the interface between premature rRNA domains II, IV and V, implying the  
251 factor associates early in biogenesis.

252 Comparison with yeast Mss116p (Del Campo et al 2009) reveals that in contrast to the arche-  
253 typal DEAD-box RNA helicase, mt-LAF2 has an 120 residue expansion in the Helicase domain  
254 2 that shields the nucleotide moiety (Fig 6B). The helicase core is in a closed conformation,  
255 tightly binding the rRNA H80 region. The rRNA is bound via its phosphate backbone, similarly  
256 to Mss116p. In the mature human mtLSU, this region forms the P-loop, a constituent of the pep-  
257 tidyl-tRNA binding site (Aibara et al., 2020). Therefore, mt-LAF2 prevents the formation of the  
258 functional site for tRNA binding in mtLSU.

259 The adenosine nucleotide is well resolved in the map, and the density in the binding pocket cor-  
260 responds to adenosine diphosphate (ADP) (Fig 6B), whereas no continuous density for  $\gamma$ -  
261 phosphate is found. The ADP is coordinated by the residues Thr150, Asp295, Arg575, and an  
262  $Mg^{2+}$  ion (Fig 6B). ATP hydrolysis was shown to promote substrate release and trigger dissociation  
263 and regeneration of the enzyme (Liu et al 2008; Henn et al 2010). However, in our structure,  
264 the helicase 2 expansion forms a tertiary junction with two  $\alpha$ - $\beta$  folds from the deactivated  
265 RPUSD4 and mt-LAF8 (Fig 6B). This architecture would interfere with the release of the ADP  
266 and substrate from mt-LAF2. The interactions further prevent mt-LAF2 disassociation from the

267 pre-mtLSU in the observed state. Therefore, RPUSD4 and mt-LAF8 play a structural role in sta-  
268 bilizing the assembly intermediate.

269

## 270 **Maturation of the L7/L12 stalk**

271 The L7/L12 stalk is a universal mobile element that associates translational protein factors with  
272 the A-site. It typically consists of the rRNA platform that connects to the flexible factor-recruit-  
273 ing series of bL12m copies. The ubiquitous ribosomal proteins uL10m, uL11m and mitochon-  
274 dria-specific mL43 link the different components together. In our structure, most of the protein  
275 constituents of the stalk are missing and others adopted conformational changes (Fig 7A).

276 In the region of the platform, at least three proteins (uL16m, bL36m, mL88) associated with the  
277 rRNA in the mature mtLSU are absent. Consistently, the rRNA platform is not folded, as the  
278 folding relies on the missing mitoribosomal proteins. Instead, the N-terminal domain of RPUSD4  
279 extends from the subunit interface to occupy part of the space left by uL16m absence (Fig 7A  
280 and B). It binds two specific assembly factors mt-LAF7 and mt-LAF8. Factor mt-LAF8 mediates  
281 further contacts with the core of the pre-mtLSU. It consists of 7-stranded beta-barrel, 12  $\alpha$ -helices,  
282 and 63-residue tail inserted into the mitoribosomal core. Our pre-mtLSU structure suggests  
283 that both mt-LAF7 and mt-LAF8 need to dissociate for the missing mitoribosomal proteins to as-  
284 semble (Fig 7A).

285 In the factor-recruiting region, instead of the terminal bL12m copies, mt-LAF15 and density cor-  
286 responding to UNK6 form a protrusion (Fig 7A). They comprise a protein continuum of at least  
287 13 helices associated with each other. This assembly is attached to the platform region through a  
288 30-residue C-terminal tail of mt-LAF15, forming a helical bundle with mL75 (Figs 7A and 7C).  
289 Overall, this protein module extends  $\sim$ 70 Å from the core in a similar fashion to the L7/L12  
290 stalk, but appears to be mutually exclusive.

291 The position of the uL10m N-terminus, which links the stalk to the body in the mature mt-LSU,  
292 is occupied by mt-LAF15 C-terminus. It interacts with mL43, resulting in its helix being bent by  
293 90° (Fig 7B). This conformational change and the lack of uL10m is correlated with  $\sim$ 15 Å shift  
294 of uL11m to occupy the formed void (Fig 7B). Nevertheless, mt-LAF15 is only peripherally as-  
295 sociated with mL43, and it cannot be excluded that the protrusion is independently replaced by  
296 the mature L7/L12 stalk.

297 Based on the structural information, the following working model for the L7/L12 stalk matura-  
298 tion, which includes dismantling, remodeling and assembly can be proposed (Fig EV5): 1)  
299 RPUSD4, which is extended from the subunit interface anchoring GTPBP7, has to be removed,  
300 2) mt-LAF7:mt-LAF8 has to be released from the ribosomal core, 3) the rRNA platform is  
301 folded, and mitoribosomal proteins uL16m, bL36m, and mL88 are recruited, 4) MRM:mt-  
302 LAF15 is removed, uL11m and mL43 then adopt their mature conformations, 5) bL10m and  
303 bL12m are finally associated to form the functional L7/L12 stalk.

304 From the density we identified three additional proteins below the L7/L12 stalk: a homolog of  
305 the human mitoribosome assembly factor MALSU1, a LYR (leucine-tyrosine-arginine) motif  
306 containing protein L0R8F8, as well as an associated mt-ACP (mt-ACP1) (Figs 1, 2 and 4). In hu-  
307 man and fungi, protein trans-acting factors in this region were shown to be involved in the last  
308 assembly stage of the mitoribosome, preventing association of the mtSSU (Brown et al 2017;  
309 Itoh et al 2020). In our structure, the module is further stabilized by mL85 to provide a steric hin-  
310 drance, consistent with the previously suggested mechanism.

311

### 312 **Assembly of the CP is linked to the subunit interface and L1 maturation via mt-ACP**

313 The most prominent architectural feature of the pre-mtLSU complex is the absence of the CP. It  
314 is a universal ribosomal element that defines the shape of the LSU and forms bridges with the  
315 SSU head. In mitoribosomes, the CP is particularly protein-rich (Amunts et 2014; Greber et al  
316 2014; Amunts et 2015; Greber et al 2015; Ramrath et al 2018; Waltz et al 2020; Tobiasson and  
317 Amunts 2020). The CP mitochondria-specific proteins were acquired in the early evolution of the  
318 mitoribosome and therefore are expected to be conserved (Petrov et al 2019).

319 In the pre-mtLSU, all the CP mitoribosomal proteins are missing and the high molecular weight  
320 assembly factors mt-LAF4 (69 kDa) and mt-LAF14 (67 kDa) are present (Figs 1 and 4, Figure  
321 EV4). Factor mt-LAF4 binds on the solvent side of the CP covering the otherwise exposed  
322 rRNA, which only engages in limited base pairing. This assembly factor is annotated as a puta-  
323 tive TruD family pseudouridine synthase. However, in our structure, it displays a two-strand an-  
324 tiparallel  $\beta$ -sheet near the catalytic site inserting into the ribosomal core and interacting with four  
325 other mitoribosomal proteins (Fig 8A). Due to this disruption of the active site the catalytic activ-  
326 ity of mt-LAF4 is likely lost. Factor mt-LAF14 is an exclusively helical protein, comprised of at  
327 least 29 helices. It binds on top of the rRNA, providing an additional protective protein cap (Figs  
328 1 and 8A).

329 Two of the mt-LAF14 helices interface with a four-helix bundle, which we identified as mt-ACP  
330 (mt-ACP2) with an average local resolution of 3.5 Å (Fig 2). Since mt-ACP proteins are known  
331 to form interactions with Leu-Tyr-Arg (LYR)-motif proteins, we compared the mt-  
332 ACP1:L0R8F8 module from the subunit interface with the CP mt-ACP2 region (Fig 8C). The  
333 helices of the LYR-motif protein L0R8F8 aligned well with a density corresponding to three hel-  
334 ices associated with the mt-ACP2. The interactions in both cases are mediated by the 4'-phos-  
335 phopantetheine (4'-PP) modification of mt-ACP, resembling the canonical interactions between  
336 mt-ACP and the LYR-motif proteins. The 4'-PP appears to be acylated as indicated by the den-  
337 sity however the exact length of the acyl chain cannot be determined (Fig 8C).

338 The presence of the 4'-PP modification, previous structural data (Zhu et al 2015; Fiedorczuk et al  
339 2016; Brown et al 2017), and the overall shape of the associated density suggest that the interact-  
340 ing partner of mtACP2 is a protein from the LYR-motif family containing at least three helices.  
341 Therefore, we searched our current and previously published (Zikova et al 2008) mass spectrom-  
342 etry data using ScanProsite (de Castro et al 2006). The hits were subjected to secondary structure

343 prediction and fitting to the density map. Our analysis singled out the protein Tb927.9.14050  
344 (UniProt ID Q38D50), which we named consistently with the adopted nomenclature, mt-LAF18.  
345 The local resolution of 3.5–4.0 Å in this region (Fig 2) allowed for 164 N-terminal residues to be  
346 built (Table EV2), which includes the three helices associated with the mt-ACP2 in proximity to  
347 the L1 stalk and two helices interacting with mt-EngA.

348 The importance of the mt-ACP2:mt-LAF18 protein module in our structure is of twofold. First, it  
349 directly binds the L1 stalk and locks it in an inward facing nonfunctional conformation (Fig 1).  
350 Second, it is involved in mt-EngA stabilization by forming a U-shaped continuum from mt-  
351 LAF14 on the solvent side of the CP to the subunit interface (Figs 1 and 4). Therefore, mt-ACP2  
352 contributes to the protein network connecting between the various functional sites. In the pre-  
353 mtSSU, mt-ACP was also identified as one of the assembly factors (Saurer et al 2019). In addi-  
354 tion, ACPs in mitochondria act as subunits of the electron transport chain (Zhu et al 2015;  
355 Fiedorczuk et al 2016) and Fe-S cluster assembly complexes (Van Vranken et al 2016). This fur-  
356 ther supports the proposed concept that mt-ACPs could be signaling molecules in an intramito-  
357 chondrial metabolic state sensing circuit (Masud et al 2019).

358 At the CP, the assembly factors cooperatively bind unwound rRNA nucleotides U934-953 (H81)  
359 Figs 8A, EV4 and Appendix S6). Remarkably, the rRNA forms a loop 25 Å in diameter that en-  
360 circles the mt-LAF4 β-sheet and mL64 C-terminal helix, both inserted from the opposite direc-  
361 tions (Fig 8B). The conserved helix of mL64 is shifted in our pre-mtLSU structure ~30 Å from  
362 the final location on the mature LSU, where it aligns the E-site. Interestingly, this is also one of  
363 the most conserved mitoribosomal proteins (Petrov et al 2019). To switch to the conserved and  
364 mature position, the extended C-tail of mL64 has to liberate from the rRNA loop and then un-  
365 dergo a large conformational shift towards the L1 stalk. Subsequently, the C-tail is inserted to its  
366 mature position, where it contacts CP components absent from the assembly intermediate. Since  
367 the L1 stalk is also shifted, the maturation towards a mature mtLSU is likely to occur in a con-  
368 certed manner upon the release of the mt-ACP2:mt-LAF18 module.

369

## 370 Discussion

371 Our cryo-EM structure reveals how the assembly factors collectively bind to the mtLSU during  
372 biogenesis. High molecular weight assembly factors shield the rRNA and form a network that  
373 spans over 180 Å, which connects the subunit interface with the maturation of the L7/L12 stalk,  
374 and the assembly of the CP and the L1 stalk. The tight binding of the mt-ACP2 with its partner  
375 proteins, one from the CP and the other from the L1 stalk, emphasizes a coordinating role. Thus,  
376 the PTC is unfolded, the L1 is anchored in its inactive conformation, and the mitoribosomal pro-  
377 teins responsible for the binding of tRNA and translational factors cannot associate due to the  
378 presence of the assembly factors at the CP and L7/L12 stalk. In addition, the exit tunnel is  
379 blocked. In this regard, the present study is in agreement with the recently published work on  
380 *Leishmania* pre-mtLSU (Soufari et al 2020), which suggested that mL67, mL71, mL77, mL78,  
381 and mL81 represent assembly factors. The N-terminus of mL71 fills the exit tunnel, and its basic

382 residues form electrostatic interactions with the rRNA that anchor the protein moiety. For a nas-  
383 cent polypeptide to emerge from the mtLSU, a continuous pathway needs to be formed from the  
384 tunnel entrance to the mitoribosomal surface, therefore mL71 N-terminus has to be removed.  
385 Together, our pre-mtLSU structure contains 22 assembly factors, several of which could also be  
386 identified in the human mitoribosome assembly pathway, including GTPBP7, MRM, RPUSD4,  
387 MALSU1, L0R8F8, mt-ACP1, and a DEAD-box RNA helicase. This allowed us to suggest a  
388 model that underpins the organization of the equivalent assembly factors in the human pre-  
389 mtLSU (Fig 9). Functionally, these assembly factors can be divided into three categories: 1)  
390 GTPBP7 and DEAD-box helicase that potentially retained their functional role of facilitating  
391 rRNA folding; 2) MRM and RPUSD4, which lost their enzymatic functions, but retained the  
392 structural role of scaffolding the assembly process; 3) MALSU1, L0R8F8, and mt-ACP1 that  
393 form a conserved module preventing premature subunit association.  
394 GTPBP7 is an essential mitoribosomal assembly factor that acts at an early assembly stage in  
395 yeast (Barrientos et al 2003; Kim and Barrientos, 2018), and also can associate with a mature  
396 LSU (Zeng et al 2018). Our analysis confirms that the residues in the nucleotide binding pocket  
397 are conserved in the GTPase domains (G1, G4), as well as in the P-loop and Switch II regions,  
398 and the nucleotide fits its pocket in our structure. DEAD-box helicase is also likely to act on an  
399 early assembly stage, as it is buried in the core of the pre-mtLSU. The DEAD-box motif is con-  
400 served, its conformation correspond to the RNA-binding state (Theissen et al 2008). This is con-  
401 sistent with the recently published structure of the pre-mtLSU (Jaskolowski et al 2020).  
402 The binding of the GTPBP7 and DEAD-box helicase is stabilized by co-localized factors, includ-  
403 ing MRM and RPUSD4. In yeast, a single amino acid substitution in the SAM pocket of MRM1  
404 abolishes its methyltransferase activity, but does not alter the formation of fully functional mi-  
405 toribosomes (Lövgren and Wikström 2001), while deletion of MRM1 leads to a defective assem-  
406 bly (Sirum-Connolly and Mason 1993). RPUSD4 is an essential gene in human cells, and it is a  
407 component of mitochondrial RNA granules (Zaganelli et al 2017). Our study points to structural  
408 roles of MRM and RPUSD4 in the assembly pathway of the mitoribosomes. MRM can also act  
409 as a docking site for the catalytically active methyltransferases MRM2/3 (Jaskolowski et al  
410 2020), involved in 2'-*O*-ribose methylation of a nucleotide in the H92 loop (Rorbach et al 2014).  
411 The preservation of the deactivated factors is likely due to the evolutionary conservation of the  
412 sequential assembly (Fig 9), where RPUSD4 also forms a platform for DEAD-box helicase, as  
413 well as further stabilizes its expanded helicase 2 domain upon ATP hydrolysis. This mechanism  
414 is analogous to the evolutionary preservation of the autonomous 5S rRNA in bacterial ribosomes  
415 due to its role in assembly of the LSU where it guides the biogenesis pathway (Huang et al  
416 2020).  
417 In conclusion, our findings provide new insights into the conserved mtLSU biogenesis process.  
418 Protein extensions of the assembly factors and additionally incorporated protein linkers stabilize  
419 the key assembly factors of the mtLSU in the functional sites. Some of the factors, such as MRM  
420 and RPUSD4 lost their original function, and serve as structural mediators for the binding of the

421 functionally active and conserved GTPBP7 and DEAD-box helicase. Therefore, the data also  
422 provides insight into the assembly of the human mitoribosome, where corresponding assembly  
423 intermediates are less stable. This showcases how the structural approach of studying stabilized  
424 intermediates is instrumental for understanding dynamic macromolecular processes that can be  
425 extrapolated to human homologs.

426  
427

428 **Figure 1. Structure of *T. brucei* pre-mtLSU with assembly factors.** Left, the overall modeled  
429 structure of the pre-mtLSU (rRNA shown as surface) with models of assembly factors (helical  
430 tubes, shades of purple) covering the subunit interface, CP, L7/L12 stalk and connecting to the  
431 L1 stalk. Right, structure of the mature mtLSU (PDB ID 6HIX) with 18 additional mitoriboso-  
432 mal proteins (shades of orange) absent from pre-mtLSU.

433

434 **Figure 2. Cryo-EM data quality.** (A) Final map colored by local resolution. (B) Models for in-  
435 dividual assembly factors and newly identified proteins colored by refined atomic B-factor.

436

437 **Figure 3. Binding of the GTPBP7 and mt-EngA to the subunit interface.** (A) GTPBP7 (yellow)  
438 is bound to RPUSD4 and MRM, which are connected to the L7/L12 stalk; mt-EngA (blue)  
439 is associated with mt-LAF2 and mt-LAF18, which are connected to the CP. (B) A short helix of  
440 mt-EngA (yellow) interacts with a flipped A894 nucleotide from H75 (white). Two GTPs in their  
441 binding sites on mt-EngA are shown as sticks. Absent GTP displayed in its binding site on  
442 GTPBP7 is shown as white sticks. The residues forming interactions between mt-EngA and  
443 GTPBP7 are shown in the top right inset. (C) Schematic representation of mt-EngA and  
444 GTPBP7 indicating the positions of the conserved GTP binding motifs.

445

446 **Figure 4. Network of interactions between the assembly factors in pre-mtLSU.** (A) Assem-  
447 bly factors shown on the background of the pre-mtLSU density map, featuring the interconnec-  
448 tion. (B) Schematic of protein-protein network. The node size represents the molecular mass of  
449 the protein. All the assembly factors are linked in a continuous network. (C) Homology search of  
450 the assembly factors. Colored squares indicate identified homologs/orthologs using *T. brucei*  
451 (green) or human (purple) assembly factors as queries. White squares indicate not-identified  
452 homologs/orthologs. The stars mark proteins, for which experimental data has been reported.

453

454 **Figure 5. Tertiary structure of rRNA in pre-mtLSU (A) and mature mtLSU (B).** Density  
455 map lowpass-filtered to 5 Å for clarity shown from the subunit interface (left) and sideview  
456 (right). Two views of rRNA related by 90° are shown with each domain in a different color. Do-  
457 main V is more structured in pre-mtLSU, and H89-93 adopt a different conformation. Domain II  
458 that is responsible for L7/L12 stalk is largely disordered.

459

460 **Figure 6. DEAD-Box helicase mt-LAF2 is buried in the pre-mtLSU in closed conformation**  
461 **with bound ADP.** (A) Relative placement of mt-LAF2 (surface) bound to rRNA (white ribbon).  
462 Helicase domain 1 (DEAD box) is light blue, helicase domain 2 (Helicase C) is blue, terminal  
463 extensions are purple. (B) Comparison with yeast Mss116p shows that rRNA is bound to mt-  
464 LAF2 via its phosphate backbone in a similar mode (yellow). Helicase domain 2 expansion in  
465 mt-LAF2 (yellow) shields the ADP, and stabilized by RPUSD4 and mt-LAF8. The density in the  
466 binding pocket (inset) corresponds to ADP and Mg<sup>2+</sup> ion. Schematic representation of mt-LAF2  
467 indicating conserved regions is shown in the bottom panel.

468

469 **Figure 7. Assembly of the L7/L12 stalk.** (A) In pre-mtLSU, RPUSD4 extends from the subunit  
470 interface to occupy the position of uL16m in the mature mtLSU. Factors mt-LAF7 and mt-LAF8  
471 are bound at the stalk base to the unfolded rRNA H41/42. Factor mt-LAF15 and an additional  
472 protein UNK6 form a protrusion similar to bL10m:bL12m. Other mitoribosomal proteins re-  
473 moved for clarity. (B) Conformational changes from pre-mtLSU (blue) to mature mtLSU (white)  
474 include mL43 and uL11m. (C) mt-LAF15, mL75, and UNK6 protein form continuum of at least  
475 13 helices that is peripherally associated.

476

477 **Figure 8. The CP assembly intermediate.** (A) Factors mt-LAF4 and mt-LAF14 form the CP in  
478 the pre-mtLSU. (B) mt-LAF4 and mL64 elements are inserted through the rRNA loop corre-  
479 sponding to H81. The conformational change of mL64 from pre-mtLSU to mature mtLSU  
480 (white) is indicated. (C) Comparison between the mt-ACP1:L0R8F8 (left) and the CP mt-  
481 ACP2:mt-LAF18 region (right). The density (white) for acylated 4'-PP is indicated. Bottom  
482 panel, comparison with mt-ACP and associated LYR-motif proteins from complex I (PDB ID  
483 5LNK) and human mitoribosome (PDB ID 5OOM) shows the canonical interactions.

484

485 **Figure 9. Schematic representation of the assembly pathway of human mtLSU.** Left, the  
486 conserved assembly factors identified in this study that are also present in human are shown in  
487 complex with the pre-mtLSU. Middle, previously reported late assembly intermediate of the hu-  
488 man mitoribosome (PDB 5OOL, Brown et al 2017) with assembled elements (relative to pre-  
489 mtLSU) shown in red. Right, mature mtLSU with fully assembled tRNA binding sites A, P, and  
490 E (PDB 6ZSG, Aibara et al 2020).

491

492 **Figure EV1.** The binding of GTPBP7 and mt-EngA at the mtLSU interface. (A) Comparison be-  
493 tween pre-mtLSU and bacterial counterparts *E. coli* 50S:EngA (PDB ID 3J8G) and *B. subtilis*  
494 45S:RbgA (PDB ID 6PPK) shows nearly identical positions of the factors on their ribosomal  
495 complexes. (B) Comparison between GTPBP7:mt-EngA module from the pre-mtLSU and super-

496 imposed bacterial counterparts combined from the two structures from (A) shows nearly identi-  
497 cal conformations. The N-terminal extension of mt-EngA (dark yellow) is buried in the mitoribo-  
498 somal core and stabilizes the binding, as well as the 275-305 region (dark yellow).

499

500 **Figure EV2.** (A) The active site of RPUSD4 (yellow) is occupied by cytidine 1010. (B) The fac-  
501 tor RPUSD4 (yellow) binds GTPBP7 (pale-yellow) via a shared  $\beta$ -sheet (circled). The methyl-  
502 transferase site of MRM does not allow for the binding of S-adenosyl methionine cofactor (white  
503 sticks and surface) due to clashes with the protein residues (inset).

504

505 **Figure EV3.** (A) N-terminal extension (yellow) of mt-EngA stabilizes helix-turn-helix (275-  
506 305), which forms interaction with mt-LAF2 on the other side (bottom right panel), and a helical  
507 bundle with mt-LAF18 that is in contact with mt-LAF14. (B) Sequence alignment of the N-ter-  
508 minus of mt-EngA shows presence of the extension in different organisms.

509

510 **Figure EV4. Binding of assembly factors to rRNA.** For each panel, rRNA is shown with an  
511 individual protein characterized in the structure, which have not been reported in the mature  
512 LSU. Bottom right panel illustrates the total RNA that is involved in the interactions (yellow)  
513 with the assembly factors. Regions and nucleotides of respective rRNA domains are presented in  
514 Table S3.

515

516 **Figure EV5. Proposed model for the L7/L12 stalk maturation.** The series of steps starts with  
517 dismantling the assembly factors from the unfolded rRNA (white dashes) that triggers rRNA  
518 folding (grey line), binding of the mitoribosomal proteins (grey) and conformational changes (ar-  
519 rows).

520

521

522 **Materials and Methods**

523 **Strains and growth conditions**

524 *T. brucei* procyclic Lister strain 427 was grown in SDM-80 medium supplemented with 10% fe-  
525 tal bovine serum. Mitochondria were isolated as described earlier Schneider (2007).  $1.5 \times 10^{11}$   
526 cells were harvested, washed in 20 mM sodium phosphate buffer pH 7.9 with 150 mM NaCl and  
527 20 mM glucose, resuspended in 1 mM Tris-HCl pH 8.0, 1 mM EDTA, and disrupted by 10  
528 strokes in 40 ml Dounce homogenizer. The hypotonic lysis was stopped by immediate addition  
529 of 1/6 volume of 1.75 M sucrose. Crude mitochondria were pelleted (15 min at 16000 xg, 4°C),  
530 resuspended in 20 mM Tris-HCl pH 8.0, 250 mM sucrose, 5 mM MgCl<sub>2</sub>, 0.3 mM CaCl<sub>2</sub> and  
531 treated with 5 µg/ml DNase I for 60 min on ice. DNase I treatment was stopped by addition of  
532 one volume of the STE buffer (20 mM Tris-HCl pH 8.0, 250 mM sucrose, 2 mM EDTA) fol-  
533 lowed by centrifugation (15 min at 16000 xg, 4°C). The pellet was resuspended in 60% Percoll  
534 in STE and loaded on the bottom of six 10-35% Percoll gradient in STE in polycarbonate tubes  
535 for SW28 rotor (Beckman). Gradients were centrifuged for 1 hour at 24000 rpm, 4°C. The mid-  
536 dle diffused phase containing mitochondrial vesicles (15-20 ml per tube) was collected, washed  
537 twice in the STE buffer, snap-frozen in liquid nitrogen and stored at -80°C.

538 **Purification of mitoribosomes**

539 Mitochondria were purified further using a stepped sucrose gradient (60 %, 32 %, 23 %, 15%) in  
540 a low ionic strength buffer (50 mM HEPES/KOH pH 7.5, 5 mM MgOAc, 2 mM EDTA). A thick  
541 pellet at the 60-32% interface was collected and lysed by mixing with 5 volumes of detergent  
542 containing lysis buffer (25 mM HEPES/KOH pH 7.5, 100 mM KCl, 15 mM MgOAc, 1.7 % Tri-  
543 ton X-100, 2 mM DTT, Complete-EDTA Free Protease Inhibitor). The lysate was centrifuged at  
544 30,000 xg twice, retaining the supernatant after each spin. The supernatant was then subjected to  
545 differential PEG precipitation; PEG 10,000 was added to reach a concentration of 1.5 % (w/v)  
546 and incubated on ice for 10 mins, followed by a spin at 30,000 xg. The supernatant was trans-  
547 ferred to a fresh tube, and PEG 10,000 was added to reach a concentration of 8 % (w/v) then in-  
548 cubated on ice for 10 mins, followed by a spin at 30,000 xg.

549 The pellet was then resuspended in 800 µl of lysis buffer and then layered onto a 34% sucrose  
550 cushion (25 mM HEPES/KOH pH 7.5, 100 mM KCl, 15 mM MgOAc, 1.0 % Triton X-100, 2  
551 mM DTT, Complete-EDTA Free Protease Inhibitor) in a TLA120.2 centrifuge tube (0.4 ml of  
552 cushion per tube). Mitoribosomes were pelleted through the cushion by centrifugation at 231,550  
553 xg for 45 min. Pelleted mitoribosomes were resuspended using a total of 100 µl of resuspension  
554 buffer (25 mM HEPES/KOH pH 7.5, 100 mM KCl, 15 mM MgOAc, 0.01 % β-DDM, 2 mM  
555 DTT). The resuspended mitoribosomes were then layered onto a continuous 15-30 % sucrose  
556 gradient and centrifuged in a TLS55 rotor for 120 min at 213,626 xg. The gradient was fraction-  
557 ated manually, and fractions containing mitoribosome as judged by the 260 nm absorbance were  
558 pooled and buffer exchanged in a centrifugal concentrator.

559 **Cryo-EM and model building**

560 For cryo-EM analysis, 3  $\mu$ L of the sample at a concentration of OD260 3.5, was applied onto a  
561 glow-discharged (20 mA for 30 seconds) holey-carbon grid (Quantifoil R2/2, copper, mesh 300)  
562 coated with continuous carbon (of  $\sim$ 3 nm thickness) and incubated for 30 seconds in a controlled  
563 environment of 100% humidity and 4 °C temperature. The grids were blotted for 3 seconds, fol-  
564 lowed by plunge-freezing in liquid ethane, using a Vitrobot MKIV (FEI/Thermofischer). The  
565 data was collected on a FEI Titan Krios (FEI/Thermofischer; Scilifelab, Stockholm, Sweden, and  
566 ESRF, Grenoble, France) transmission electron microscope operated at 300 keV, using C2 aper-  
567 ture of 70  $\mu$ m; slit width of 20 eV on a GIF quantum energy filter (Gatan). A K2 Summit detec-  
568 tor (Gatan) was used to collect images at a pixel size of 1.05  $\text{\AA}$  (magnification of 130,000X) with  
569 a dose of  $\sim$ 35 electrons/ $\text{\AA}^2$  fractionated over 20 frames. A defocus range of 0.8 to 3.5  $\mu$ m was  
570 applied.

571 19,158 micrographs (after bad images were removed based on real and reciprocal space features)  
572 were collected across 5 non-consecutive data acquisition sessions and processed together using  
573 RELION. 896,263 particles were picked using Warp and coordinates were imported into  
574 RELION for particle extraction at an initial binning factor of two. The particles were subjected to  
575 supervised 3D classification using references generated previously in a screening dataset, which  
576 was started based on the *T. brucei* cytosolic ribosome as an initial model. This crude separation  
577 classified the 207,788 particles as mtLSU-like, and the remaining as mature mtLSU-like, SSU-  
578 like or monosomes. This subset was subjected to auto-refinement separately to improve the an-  
579 gular assignments and then classified further using fine-angular searches with a solvent mask ap-  
580 plied. From the mtLSU-like particles, 32,339 particles were retained as pre-mtLSU of good qual-  
581 ity and the rest were discarded as non-particles. The retained pre-mtLSUs were then subjected to  
582 auto-refinement once more to improve the angles further, this time applying a solvent mask dur-  
583 ing the refinement procedure, and then the 3D reconstructions obtained were used as a reference  
584 for CTF refinement to improve the reconstruction. The final map was then estimated for local  
585 resolution using RELION and sharpened with a B-factor appropriate for the reconstruction as es-  
586 timated automatically using the postprocessing procedure.

587 Model building was done using *Coot* 0.9 (Emsley et al 2010). First the model of the mature  
588 mtLSU (PDB ID:6HIX) was fitted to the density. Chains present in the pre-mtLSU were then in-  
589 dividually fitted and locally refined. Additional chains were first identified using information  
590 from sidechain densities. First the map density, chemical environment and sidechain interactions  
591 were used to create probable sequences. Those sequences were then queried against *T. brucei*  
592 specific databases; potential hits were evaluated individually and finally assigned. Models were  
593 modeled de-novo. All models were refined iteratively using PHENIX (Liebschner et al 2019) re-  
594 alspace refinement and validated using MolProbity (Williams et al 2018). The data collection,  
595 model refinement and validation statistics are presented in Table S1. All figures were prepared  
596 either in Chimera (Pettersen et al 2004) or ChimeraX (Goddard et al 2018) with additional  
597 graphical elements created using Inkscape.

598 **Search for homologs of assembly factors and sequence alignments**

599 Homologs of assembly factors found in our pre-mtLSU and identified by cryo-EM were  
600 searched in the NCBI protein database with Position-Specific Iterated BLAST (Altschul et al  
601 1997) using sequences of individual factors from *T. brucei* as queries. The searches were tar-  
602 getted against selected genera. Sequence alignments were generated with the MUSCLE (Larkin et  
603 al 2007) algorithm in Geneious (Biomatters Ltd., New Zealand) and corrected manually.  
604

## 605 **Data availability**

606 The electron density map has been deposited in EMDB under accession code EMD-11845. The  
607 model has been deposited in PDB under accession code 7AOI. All data is available in the paper  
608 or Supplementary Information.

609

## 610 **Acknowledgements**

611 We acknowledge the ESRF beamline CM01 for provision of beam time, and would like to thank  
612 especially Eaazhisai Kandiah and Michael Hons for the excellent continuous support. We also  
613 thank the SciLifeLab cryo-EM and mass spectrometry facilities, Nikhil Jain for comments. This  
614 work was supported by the Swedish Foundation for Strategic Research (FFL15:0325), Ragnar  
615 Söderberg Foundation (M44/16), European Research Council (ERC-2018-StG-805230), Knut  
616 and Alice Wallenberg Foundation (2018.0080), EMBO Young Investigator Program to A.A., and  
617 by and by Czech Science Foundation (18-17529S), ERD fund  
618 (CZ.02.1.01/0.0/0.0/16\_019/0000759) to A.Z., and by Czech Science Foundation (20-04150Y)  
619 to O.G. The cryo-EM facility is funded by the Knut and Alice Wallenberg, Family Erling  
620 Persson, and Kempe foundations.

621

## 622 **Author contributions**

623 Project conceptualization: OG, AZ, AA; Sample preparation for cryo-EM: OG, SA, AA; Data  
624 acquisition and processing: SA; Model building and validation: VT, OG, SA, RB; Structural data  
625 interpretation: VT, OG, AA; Manuscript writing and figure preparation: VT, OG, SA, RB, AZ,  
626 AA.

627

## 628 **References**

629 Achila, D., Gulati, M., Jain, N. & Britton, R. A. (2012) Biochemical characterization of  
630 ribosome assembly GTPase RbgA in *Bacillus subtilis*, *J Biol Chem.* 287, 8417-23  
631 Altschul, S. F., Madden, T. L., Schäffer, A. A., Zhang, J., Zhang, Z., Miller, W., & Lipman, D. J.  
632 (1997). Gapped BLAST and PSI-BLAST: a new generation of protein database search  
633 programs. *Nucleic acids research*, 25(17), 3389-3402  
634 Amunts, A., Brown, A., Bai, X. C., Llacer, J. L., Hussain, T., Emsley, P., Long, F., Murshudov,  
635 G., Scheres, S. H. & Ramakrishnan, V. (2014) Structure of the yeast mitochondrial large  
636 ribosomal subunit, *Science*. 343, 1485-9

637 Amunts, A., Brown, A., Toots, J., Scheres, S. H. W. & Ramakrishnan, V. (2015) Ribosome. The  
638 structure of the human mitochondrial ribosome, *Science*. 348, 95-98

639 Aibara, S., Singh, V., Modelska, A., & Amunts, A. (2020). Structural basis of mitochondrial  
640 translation. *eLife*, 9, e58362

641 Antonicka, H. and Shoubridge, E.A., 2015. Mitochondrial RNA granules are centers  
642 for posttranscriptional RNA processing and ribosome biogenesis. *Cell reports*, 10(6),  
643 pp.920-932

644 Barrientos, A., Korr, D., Barwell, K. J., Sjulsen, C., Gajewski, C. D., Manfredi, G., Ackerman, S.  
645 & Tzagoloff, A. (2003) MTG1 codes for a conserved protein required for mitochondrial  
646 translation, *Mol Biol Cell*. 14, 2292-302

647 Bogenhagen, D.F., Martin, D.W. and Koller, A., 2014. Initial steps in RNA  
648 processing and ribosome assembly occur at mitochondrial DNA nucleoids. *Cell*  
649 *metabolism*, 19(4), pp.618-629

650 Brown, A., Rathore, S., Kimanius, D., Aibara, S., Bai, X. C., Rorbach, J., Amunts, A. &  
651 Ramakrishnan, V. (2017) Structures of the human mitochondrial ribosome in native states of  
652 assembly, *Nat Struct Mol Biol*. 24, 866-9

653 Couvillion MT, Soto IC, Shipkovenska G, Churchman LS., 2016. Synchronized mitochondrial  
654 and cytosolic translation programs. *Nature*, 533(7604):499–503

655 Davis, J. H., Tan, Y. Z., Carragher, B., Potter, C. S., Lyumkis, D. & Williamson, J. R. (2016)  
656 Modular Assembly of the Bacterial Large Ribosomal Subunit, *Cell*. 167, 1610-1622 e15

657 Davis, J. H. & Williamson, J. R. (2017) Structure and dynamics of bacterial ribosome  
658 biogenesis, *Philos Trans R Soc Lond B Biol Sci*. 372

659 De Castro, E., Sigrist, C. J., Gattiker, A., Bulliard, V., Langendijk-Genevaux, P. S., Gasteiger,  
660 E., ... & Hulo, N. (2006). ScanProsite: detection of PROSITE signature matches and ProRule-  
661 associated functional and structural residues in proteins. *Nucleic acids research*, 34(suppl\_2),  
662 W362-W365

663 De Silva, D., Tu, Y.T., Amunts, A., Fontanesi, F. and Barrientos, A., 2015. Mitochondrial  
664 ribosome assembly in health and disease. *Cell Cycle*, 14(14), pp.2226-2250

665 Del Campo, M. & Lambowitz, A. M. 2009. Structure of the yeast DEAD-box protein Mss116p  
666 reveals two wedges that crimp RNA. *Mol. Cell* 35, 598–609.

667 Emsley, P., Lohkamp, B., Scott, W. G. & Cowtan, K. (2010) Features and development of Coot.  
668 *Acta Crystallogr. D Biol. Crystallogr.* 66, 486–501

669 Fiedorczuk, K., Letts, J. A., Degliesposti, G., Kaszuba, K., Skehel, M., & Sazanov, L. A. (2016).  
670 Atomic structure of the entire mammalian mitochondrial complex I. *Nature*, 538(7625), 406-410

671 Greber, B. J., Boehringer, D., Leibundgut, M., Bieri, P., Leitner, A., Schmitz, N., Aebersold, R.  
672 & Ban, N. (2014) The complete structure of the large subunit of the mammalian mitochondrial  
673 ribosome, *Nature*. 515, 283-6

674 Greber, B. J., Bieri, P., Leibundgut, M., Leitner, A., Aebersold, R., Boehringer, D. & Ban, N.  
675 (2015) Ribosome. The complete structure of the 55S mammalian mitochondrial ribosome,  
676 *Science*. 348, 303-8

677 Greber, B. J. & Ban, N. (2016) Structure and Function of the Mitochondrial Ribosome, *Annu Rev Biochem.* 85, 103-32.

678

679 Goddard, T.D., Huang, C.C., Meng, E.C., Pettersen, E.F., Couch, G.S., Morris, J.H. and Ferrin, T.E. (2018) UCSF ChimeraX: Meeting modern challenges in visualization and analysis. *Protein Science* 27, 14–25.

680

681

682 Gulati, M., Jain, N., Anand, B., Prakash, B., & Britton, R. A. (2013). Mutational analysis of the ribosome assembly GTPase RbgA provides insight into ribosome interaction and ribosome-stimulated GTPase activation. *Nucleic acids research*, 41(5), 3217-3227.

683

684

685 Gutgsell, N. S., Deutscher, M. P. & Ofengand, J. (2005) The pseudouridine synthase RluD is required for normal ribosome assembly and function in *Escherichia coli*, *RNA*. 11, 1141-52.

686

687 Gutgsell, N. S., Del Campo, M., Raychaudhuri, S. & Ofengand, J. (2001) A second function for pseudouridine synthases: A point mutant of RluD unable to form pseudouridines 1911, 1915, and 688 1917 in *Escherichia coli* 23S ribosomal RNA restores normal growth to an RluD-minus strain, 689 *RNA*. 7, 990-8.

690

691 Henn, A., Cao, W., Licciardello, N., Heitkamp, S. E., Hackney, D. D., & Enrique, M. (2010). 692 Pathway of ATP utilization and duplex rRNA unwinding by the DEAD-box helicase, 693 DbpA. *Proceedings of the National Academy of Sciences*, 107(9), 4046-4050.

694

695 Huang, S., Aleksashin, N. A., Loveland, A. B., Klepacki, D., Reier, K., Kefi, A., Szal, T., 696 Remme, J., Jaeger, L., Vázquez-Laslop, N. & Korostelev, A. A. (2020). Ribosome engineering 697 reveals the importance of 5S rRNA autonomy for ribosome assembly. *Nature Communications*, 11(1), 1-13.

698

699 Hori H. Transfer RNA methyltransferases with a SpoU-TrmD (SPOUT) fold and their modified nucleosides in tRNA. (2017), *Biomolecules*, 7(1), 23.

700

701 Jaskolowski, M., Ramrath, D. J., Bieri, P., Niemann, M., Mattei, S., Calderaro, S., ... & Ban, N. 702 (2020). Structural insights into the mechanism of mitoribosomal large subunit biogenesis. *Molecular cell*, 79(4), 629-644.

703

704 Jomaa, A., Jain, N., Davis, J. H., Williamson, J. R., Britton, R. A. & Ortega, J. (2014) Functional domains of the 50S subunit mature late in the assembly process, *Nucleic Acids Res.* 42, 3419-35

705

706 Kim, H. J., & Barrientos, A. (2018). MTG1 couples mitoribosome large subunit assembly with intersubunit bridge formation. *Nucleic acids research*, 46(16), 8435-8453.

707

708 Kimanius, D., Forsberg, B. O., Scheres, S. H. & Lindahl, E. (2016) Accelerated cryo-EM structure determination with parallelisation using GPUs in RELION-2, *Elife*. 5

709

710 Itoh, Y., Naschberger, A., Mortezaei, N., Herrmann, J. & Amunts, A. (2020) Analysis of 711 translating mitoribosome reveals functional characteristics of protein synthesis in mitochondria of fungi, *Nature Communications* 11, 5187.

712

713 Larkin, M. A., Blackshields, G., Brown, N. P., Chenna, R., McGettigan, P. A., McWilliam, H., ... & Thompson, J. D. (2007). Clustal W and Clustal X version 2.0. *bioinformatics*, 23(21), 2947-2948.

714

715 Li, N., Chen, Y., Guo, Q., Zhang, Y., Yuan, Y., Ma, C., Deng, H., Lei, J. & Gao, N. (2013) 716 Cryo-EM structures of the late-stage assembly intermediates of the bacterial 50S ribosomal 717 subunit, *Nucleic Acids Res.* 41, 7073-83.

718 Liebschner, D., Afonine, P.V., Baker, M.L., Bunkóczki, G., Chen, V.B., Croll, T.I., Hintze, B.,  
719 Hung, L.W., Jain, S., McCoy, A.J. and Moriarty, N.W. (2019) Macromolecular structure  
720 determination using X-rays, neutrons and electrons: recent developments in Phenix. *Acta  
721 Crystallogr D Struct Biol* 75, 861–877.

722 Liu, F., Putnam, A., & Jankowsky, E. (2008). ATP hydrolysis is required for DEAD-box protein  
723 recycling but not for duplex unwinding. *Proceedings of the National Academy of  
724 Sciences*, 105(51), 20209-20214.

725 Lövgren J. M., Wikström P. M. (2001). The rlmB gene is essential for formation of Gm2251 in  
726 23S rRNA but not for ribosome maturation in *Escherichia coli*. *J. Bacteriol.* 183, 6957–6960.

727 Masud, A.J., Kastaniotis, A.J., Rahman, M.T., Autio, K.J. and Hiltunen, J.K. (2019).  
728 Mitochondrial acyl carrier protein (ACP) at the interface of metabolic state sensing and  
729 mitochondrial function. *Biochimica et Biophysica Acta (BBA)-Molecular Cell Research*, 1866,  
730 118540.

731 Ni, X., Davis, J. H., Jain, N., Razi, A., Benlekbir, S., McArthur, A. G., Rubinstein, J. L., Britton,  
732 R. A., Williamson, J. R. & Ortega, J. (2016) YphC and YsxC GTPases assist the maturation of  
733 the central protuberance, GTPase associated region and functional core of the 50S ribosomal  
734 subunit, *Nucleic Acids Res.* 44, 8442-55.

735 Nikolay, R., Hilal, T., Qin, B., Mielke, T., Burger, J., Loerke, J., Textoris-Taube, K., Nierhaus,  
736 K. H. & Spahn, C. M. T. (2018) Structural Visualization of the Formation and Activation of the  
737 50S Ribosomal Subunit during In Vitro Reconstitution, *Mol Cell.* 70, 881-893 e3

738 Ott, M., Amunts, A., & Brown, A., 2016. Organization and regulation of mitochondrial protein  
739 synthesis. *Annual Review of Biochemistry*, 85, 77-101.

740 Pausch, P., Steinchen, W., Wieland, M., Klaus, T., Freibert, S. A., Altegoer, F., Wilson, D. N. &  
741 Bange, G. (2018) Structural basis for (p)ppGpp-mediated inhibition of the GTPase RbgA, *J Biol  
742 Chem.* 293, 19699-19709.

743 Pearce, S. F., Rebelo-Guiomar, P., D’Souza, A. R., Powell, C. A., Van Haute, L., & Minczuk, M.  
744 (2017). Regulation of mammalian mitochondrial gene expression: recent advances. *Trends in  
745 biochemical sciences*, 42(8), 625-639.

746 Pettersen, E.F., Goddard, T.D., Huang, C.C., Couch, G.S., Greenblatt, D.M., Meng, E.C. and  
747 Ferrin, T.E. (2004) UCSF Chimera – a visualization system for exploratory research and analy-  
748 sis. *Journal of Computational Chemistry* 25, 1605–1612.

749 Petrov, A. S., Wood, E. C., Bernier, C. R., Norris, A. M., Brown, A. & Amunts, A. (2019)  
750 Structural Patching Fosters Divergence of Mitochondrial Ribosomes, *Mol Biol Evol.* 36, 207-219

751 Ramrath, D. J. F., Niemann, M., Leibundgut, M., Bieri, P., Prange, C., Horn, E. K., Leitner, A.,  
752 Boehringer, D., Schneider, A. & Ban, N. (2018) Evolutionary shift toward protein-based  
753 architecture in trypanosomal mitochondrial ribosomes, *Science* 362.

754 Rorbach, J., Boesch, P., Gammie, P. A., Nicholls, T. J., Pearce, S. F., Patel, D., Hauser, A.,  
755 Perocchi, F. & Minczuk, M. (2014). MRM2 and MRM3 are involved in biogenesis of the large  
756 subunit of the mitochondrial ribosome. *Molecular biology of the cell*, 25(17), 2542-2555.

757 Saurer, M., Ramrath, D. J. F., Niemann, M., Calderaro, S., Prange, C., Mattei, S., Scaiola, A.,  
758 Leitner, A., Bieri, P., Horn, E. K., Leibundgut, M., Boehringer, D., Schneider, A. & Ban, N.  
759 (2019) Mitoribosomal small subunit biogenesis in trypanosomes involves an extensive assembly  
760 machinery, *Science*. 365, 1144-1149.

761 Seffouh, A., Jain, N., Jahagirdar, D., Basu, K., Razi, A., Ni, X., Guarne, A., Britton, R. A. &  
762 Ortega, J. (2019) Structural consequences of the interaction of RbgA with a 50S ribosomal  
763 subunit assembly intermediate, *Nucleic Acids Res.* 47, 10414-10425.

764 Schneider, A., Charriere, F., Pusnik, M. & Horn, E. K. (2007) Isolation of mitochondria from  
765 procyclic *Trypanosoma brucei*, *Methods Mol Biol.* 372, 67-80.

766 Sirum-Connolly K., Mason T. L. (1993). Functional requirement of a site-specific ribose  
767 methylation in ribosomal RNA. *Science* 262, 1886–1889.

768 Soufari, H., Waltz, F., Parrot, C., Durrieu-Gaillard, S., Bochler, A., Kuhn, L., Sissler, M. &  
769 Hashem, Y. (2020). Structure of the mature kinetoplastids mitoribosome and insights into its  
770 large subunit biogenesis. *Proceedings of the National Academy of Sciences* 117 29851-29861.

771 Tegunov, D. & Cramer, P. (2019) Real-time cryo-electron microscopy data preprocessing with  
772 Warp, *Nat Methods.* 16, 1146-1152.

773 Theissen, B., Karow, A. R., Köhler, J., Gubaev, A., & Klostermeier, D. (2008). Cooperative  
774 binding of ATP and RNA induces a closed conformation in a DEAD box RNA helicase.  
775 *Proceedings of the National Academy of Sciences*, 105(2), 548-553.

776 Tobiasson, V. & Amunts, A. (2020) Ciliate mitoribosome illuminates evolutionary steps of  
777 mitochondrial translation, *eLife.* 9, e59264.

778 Van Vranken, J.G., Jeong, M.Y., Wei, P., Chen, Y.C., Gygi, S.P., Winge, D.R. and Rutter, J.  
779 (2016). The mitochondrial acyl carrier protein (ACP) coordinates mitochondrial fatty acid  
780 synthesis with iron sulfur cluster biogenesis. *Elife*, 5, e17828.

781 Waltz, F., Soufari, H., Bochler, A., Giege, P. & Hashem, Y. (2020) Cryo-EM structure of the  
782 RNA-rich plant mitochondrial ribosome, *Nat Plants.* 6, 377-383.

783 Williams, JS. et al. (2018) MolProbity: More and better reference data for improved all-atom  
784 structure validation. *Protein Science* 27, 293-315.

785 Xing, Z., Ma, W. K., & Tran, E. J. (2019). The DDX5/Dbp2 subfamily of DEAD-box RNA hel-  
786 icases. *Wiley Interdisciplinary Reviews: RNA*, 10(2), e1519.

787 Zaganelli, S., Rebelo-Guiomar, P., Maundrell, K., Rozanska, A., Pierredon, S., Powell, C. A.,  
788 Jourdain, A.A., Hulo, N., Lightowers, R.N., Chrzanowska-Lightowers, Z.M., & Minczuk, M.  
789 (2017). The pseudouridine synthase RPUSD4 is an essential component of mitochondrial RNA  
790 granules. *Journal of Biological Chemistry*, 292(11), 4519-4532.

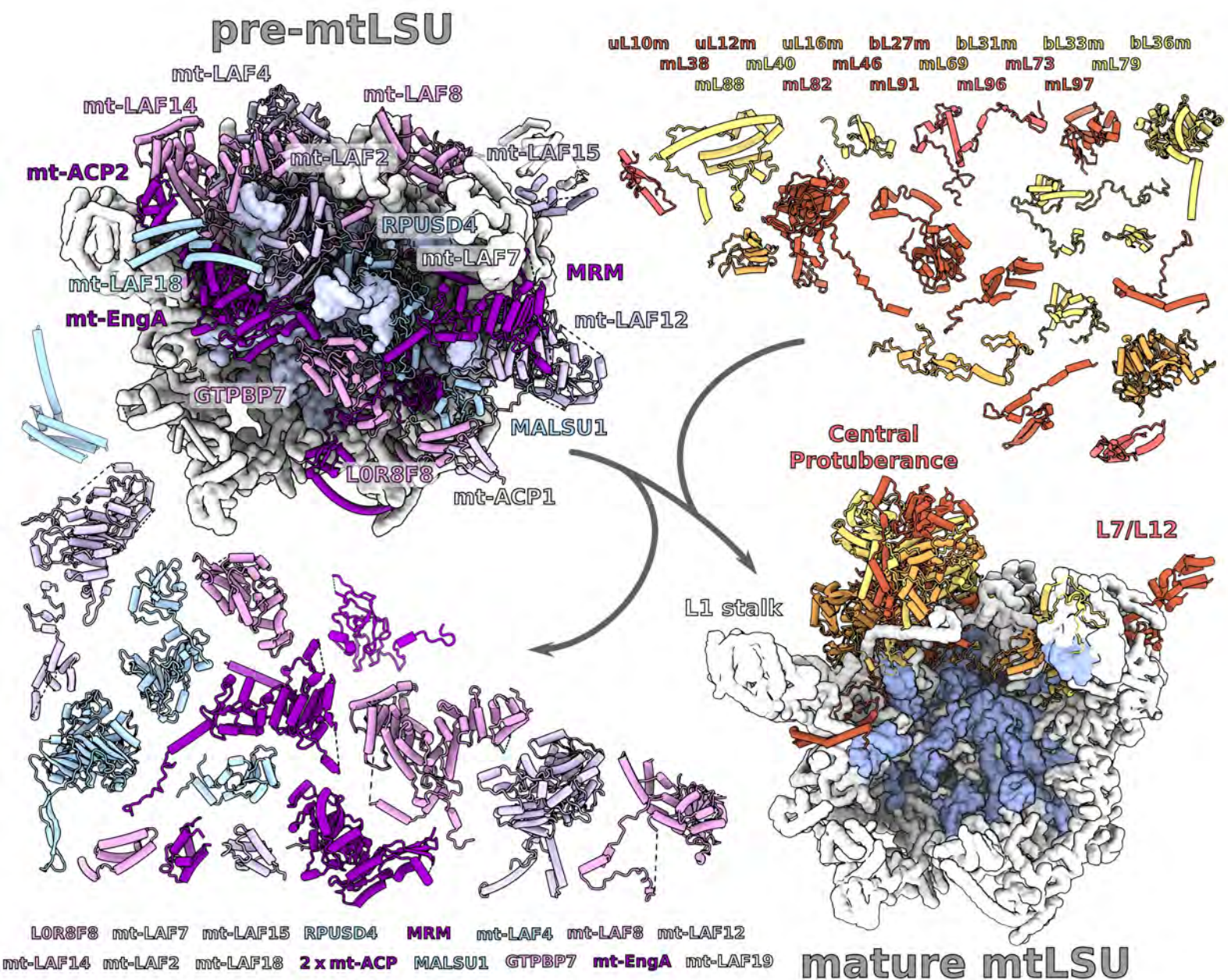
791 Zeng, R., Smith, E., & Barrientos, A. (2018). Yeast mitoribosome large subunit assembly pro-  
792 ceeds by hierarchical incorporation of protein clusters and modules on the inner membrane. *Cell  
793 metabolism*, 27(3), 645-656.

794 Zikova, A., Panigrahi, A. K., Dalley, R. A., Acestor, N., Anupama, A., Ogata, Y., Myler, P. J. &  
795 Stuart, K. (2008) *Trypanosoma brucei* mitochondrial ribosomes: affinity purification and  
796 component identification by mass spectrometry, *Mol Cell Proteomics.* 7, 1286-96.

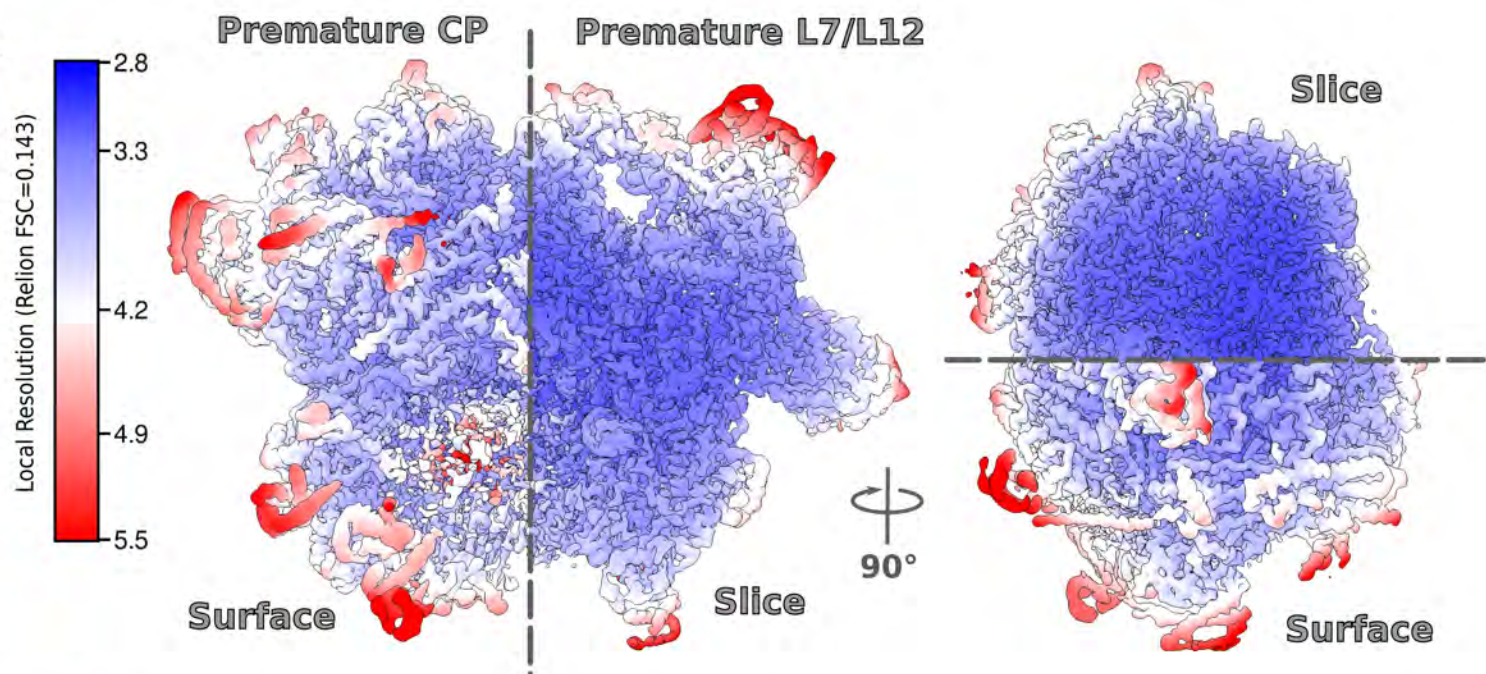
797 Zhang, X., Yan, K., Zhang, Y., Li, N., Ma, C., Li, Z., Zhang, Y., Feng, B., Liu, J., Sun, Y., Xu,  
798 Y., Lei, J. & Gao, N. (2014) Structural insights into the function of a unique tandem GTPase  
799 EngA in bacterial ribosome assembly, *Nucleic Acids Res.* 42, 13430-9.

800 Zivanov, J., Nakane, T., Forsberg, B. O., Kimanis, D., Hagen, W. J., Lindahl, E., Scheres, S. H.  
801 (2018) New tools for automated high-resolution cryo-EM structure determination in RELION-  
802 3, *eLife* 7.

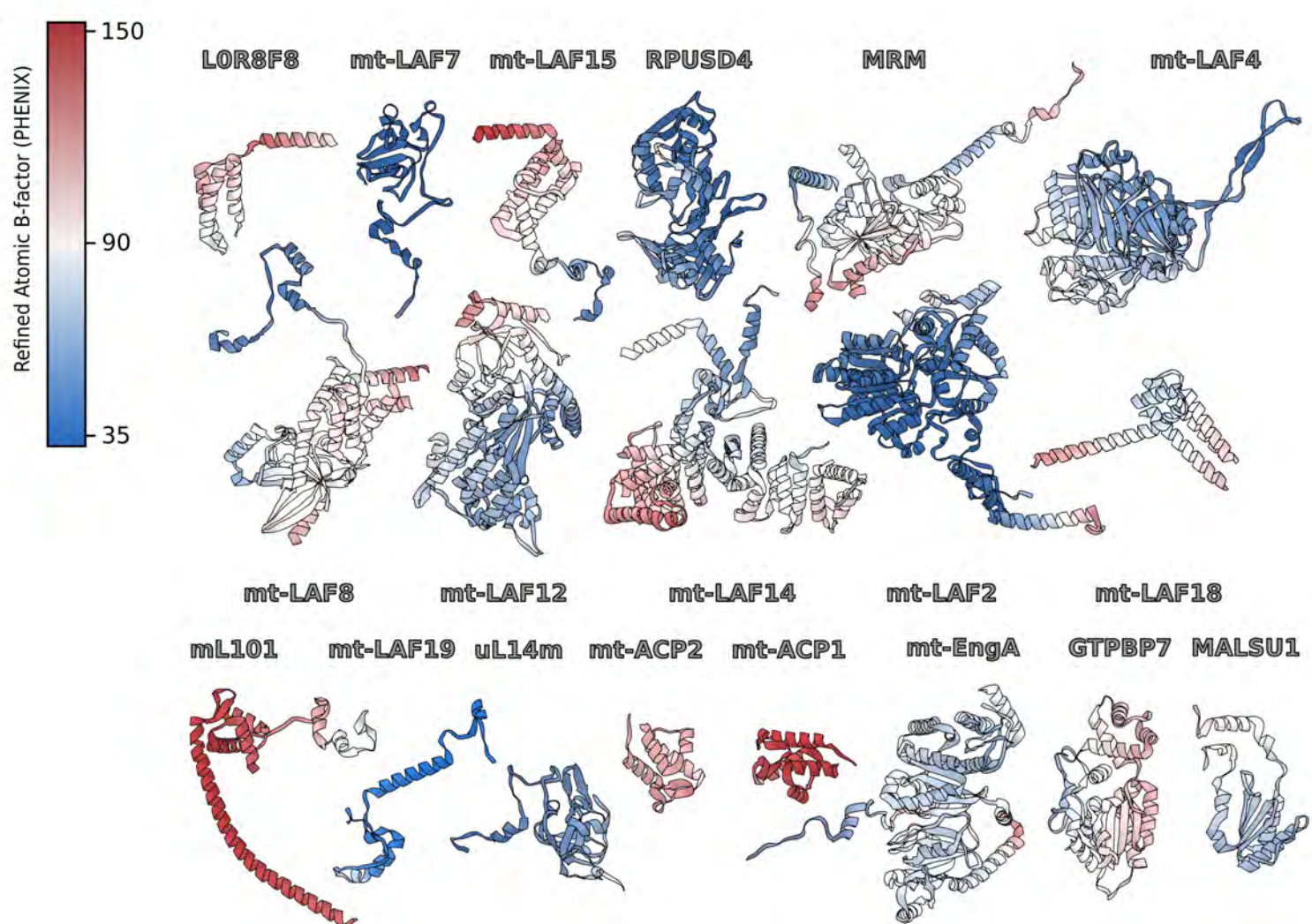
803 Zhu, J., King, M.S., Yu, M., Klipcan, L., Leslie, A.G. and Hirst, J. (2015) Structure of  
804 subcomplex I $\beta$  of mammalian respiratory complex I leads to new supernumerary subunit  
805 assignments. *Proceedings of the National Academy of Sciences*, 112, 12087-12092.



A

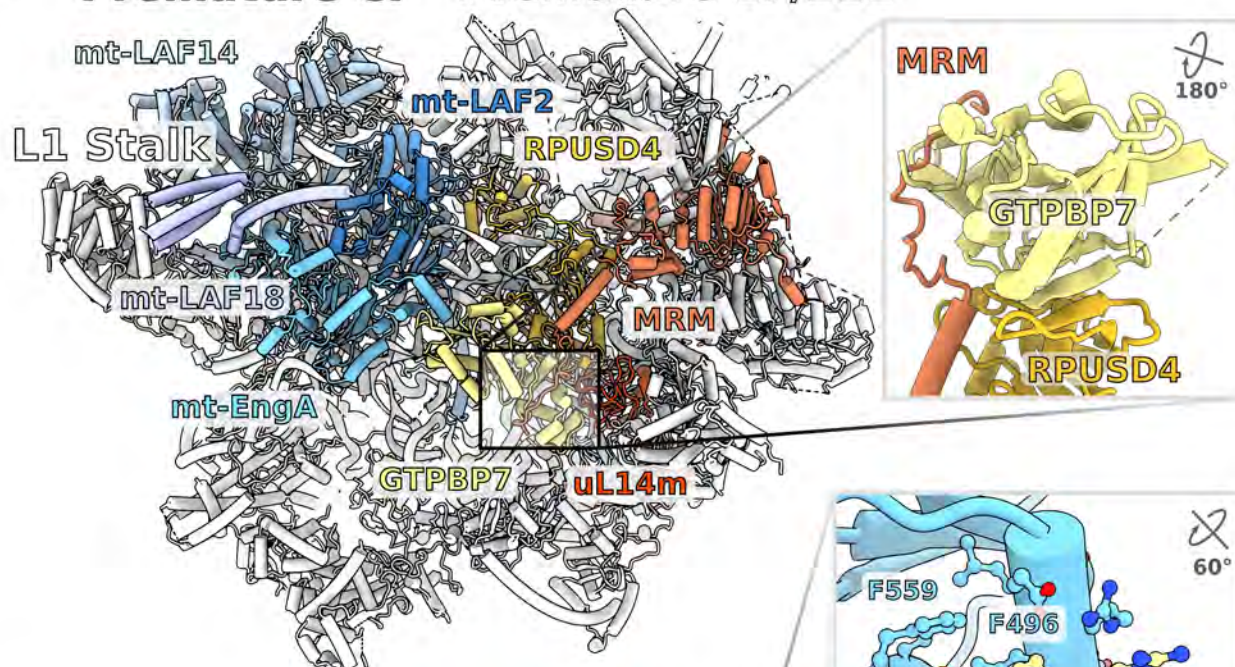


B

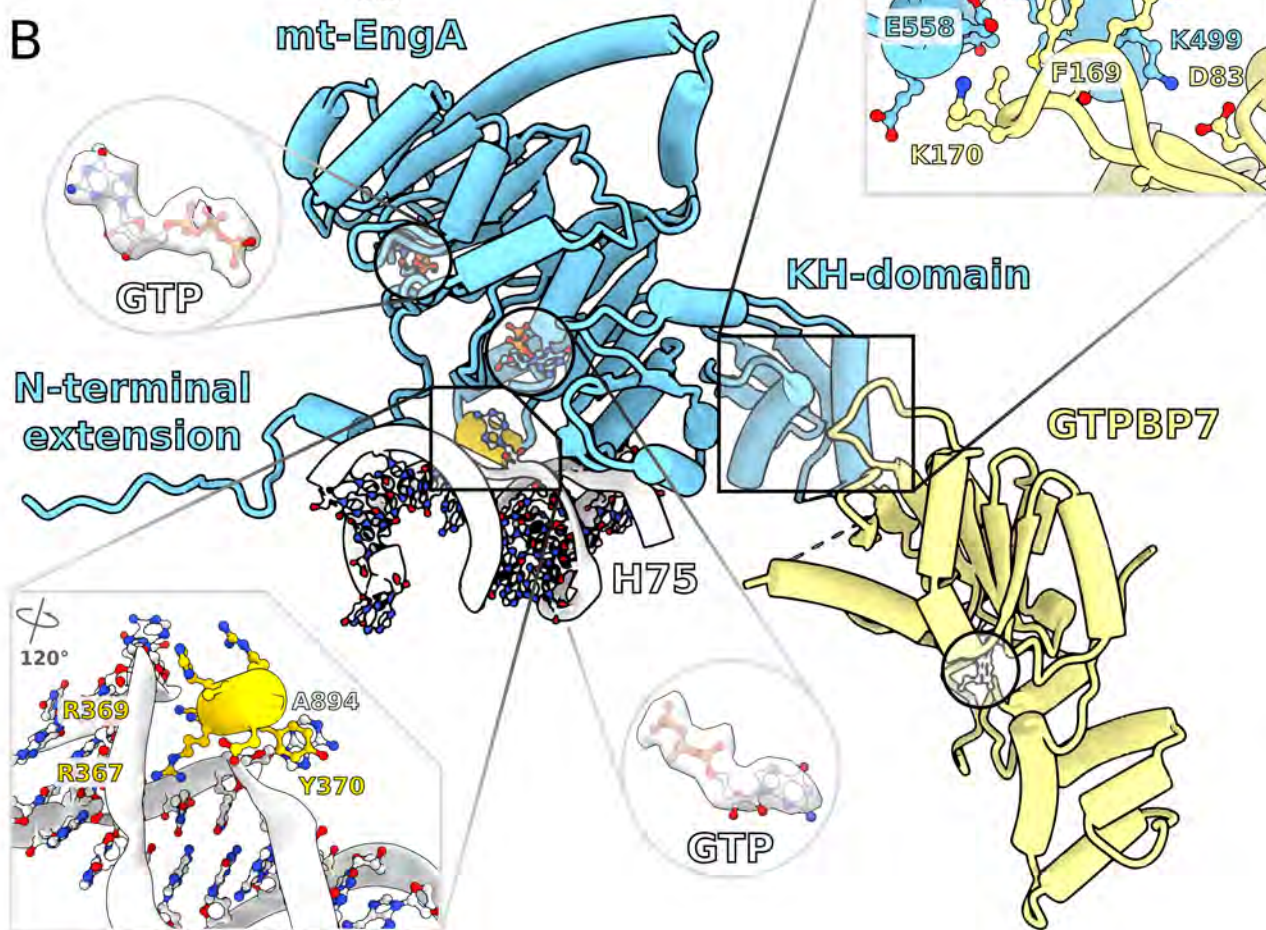


A

Premature CP      Premature L7/L12

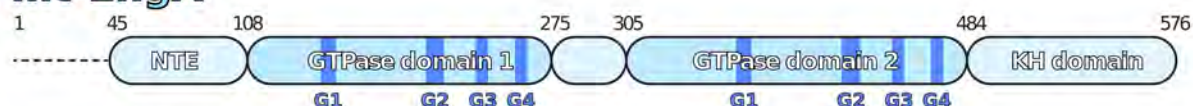


B



C

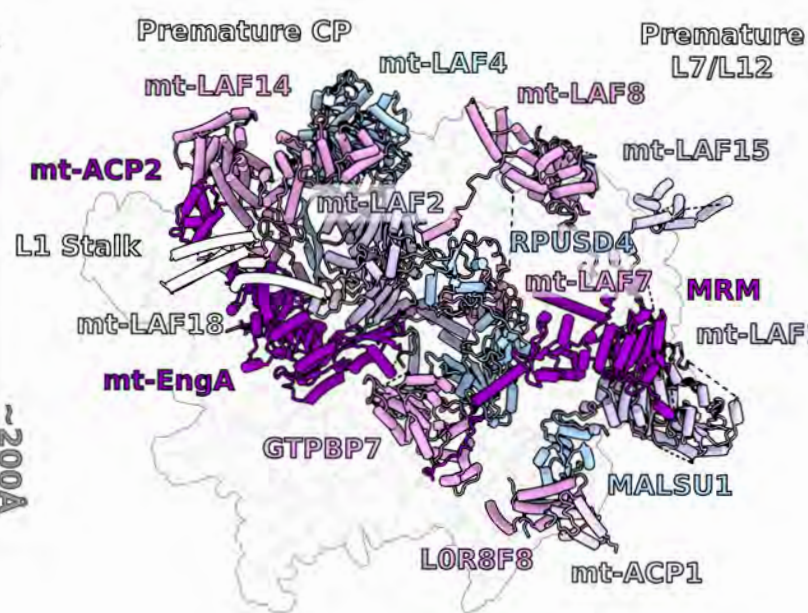
mt-EngA



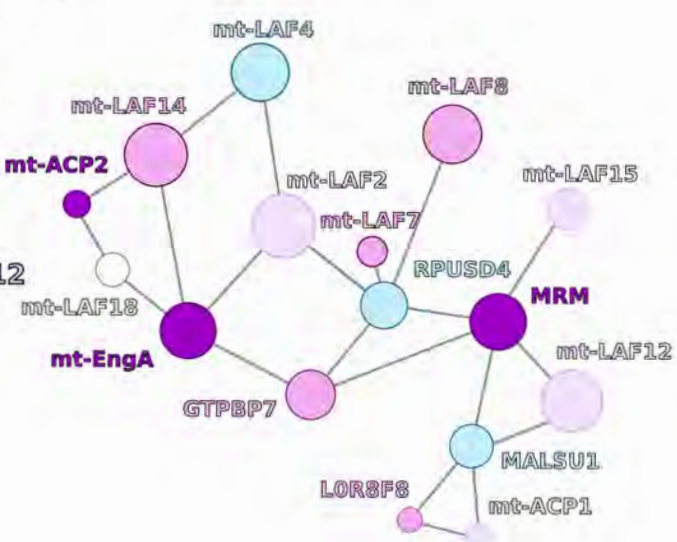
GTPBP7



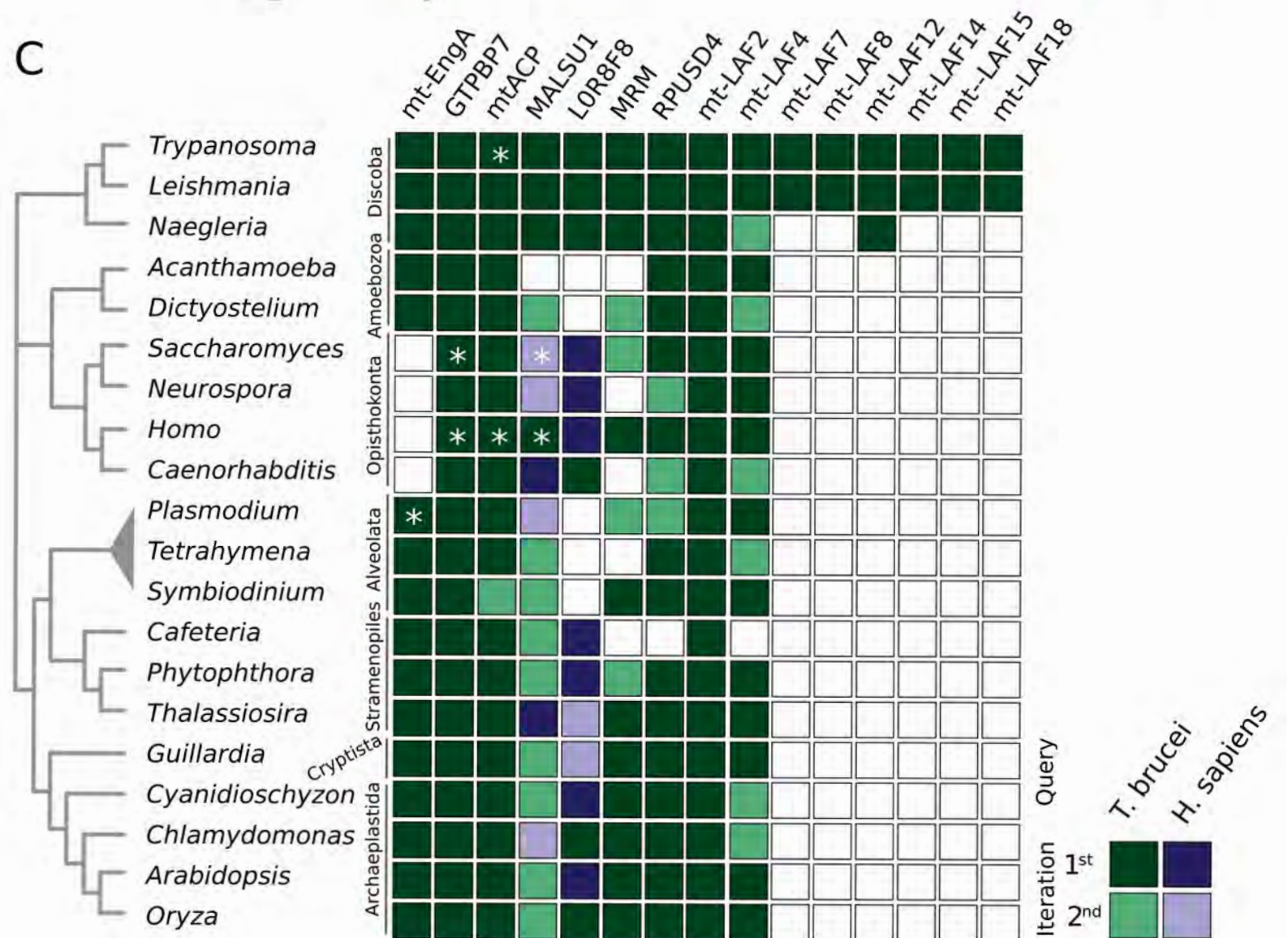
A

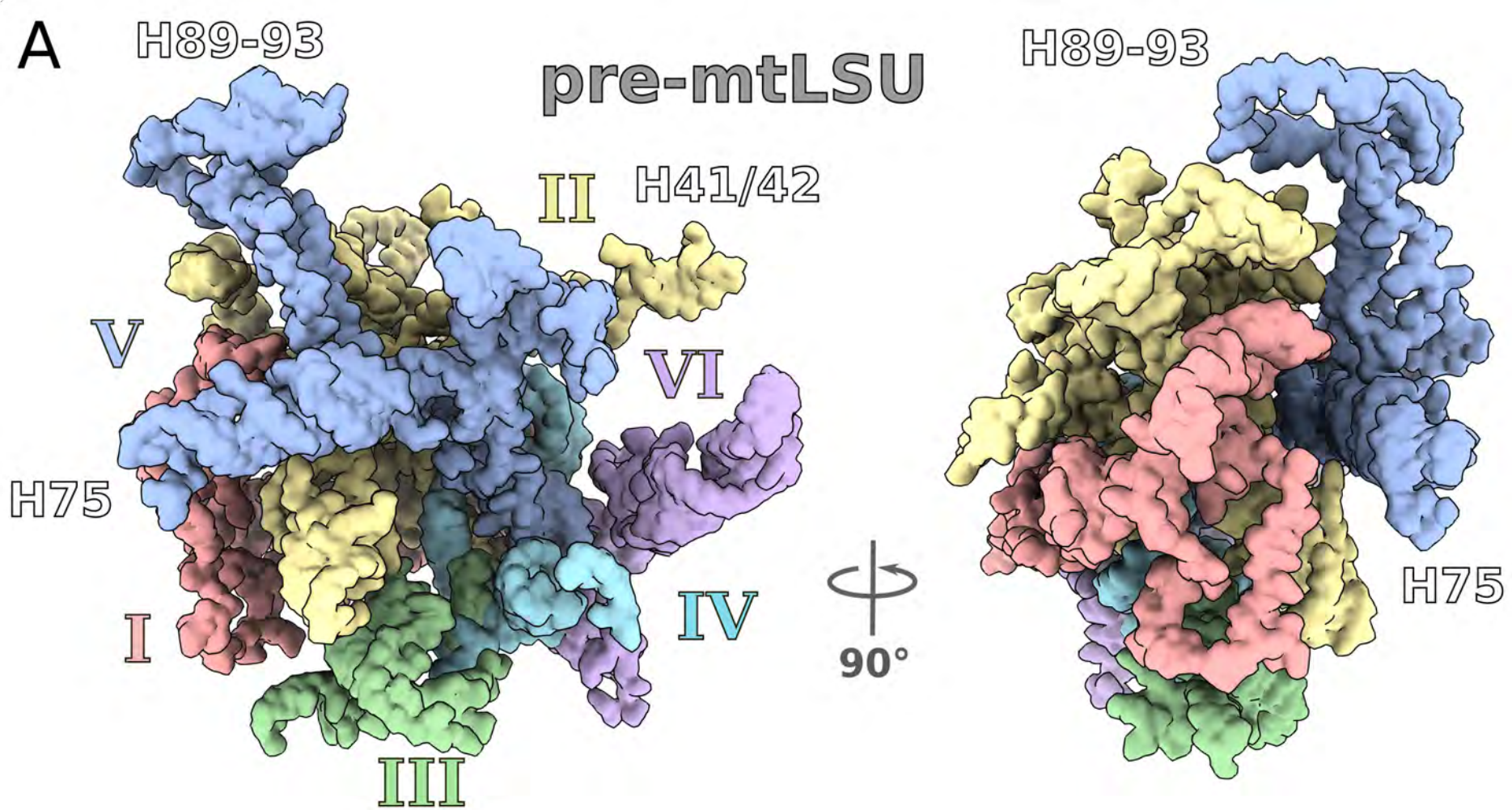
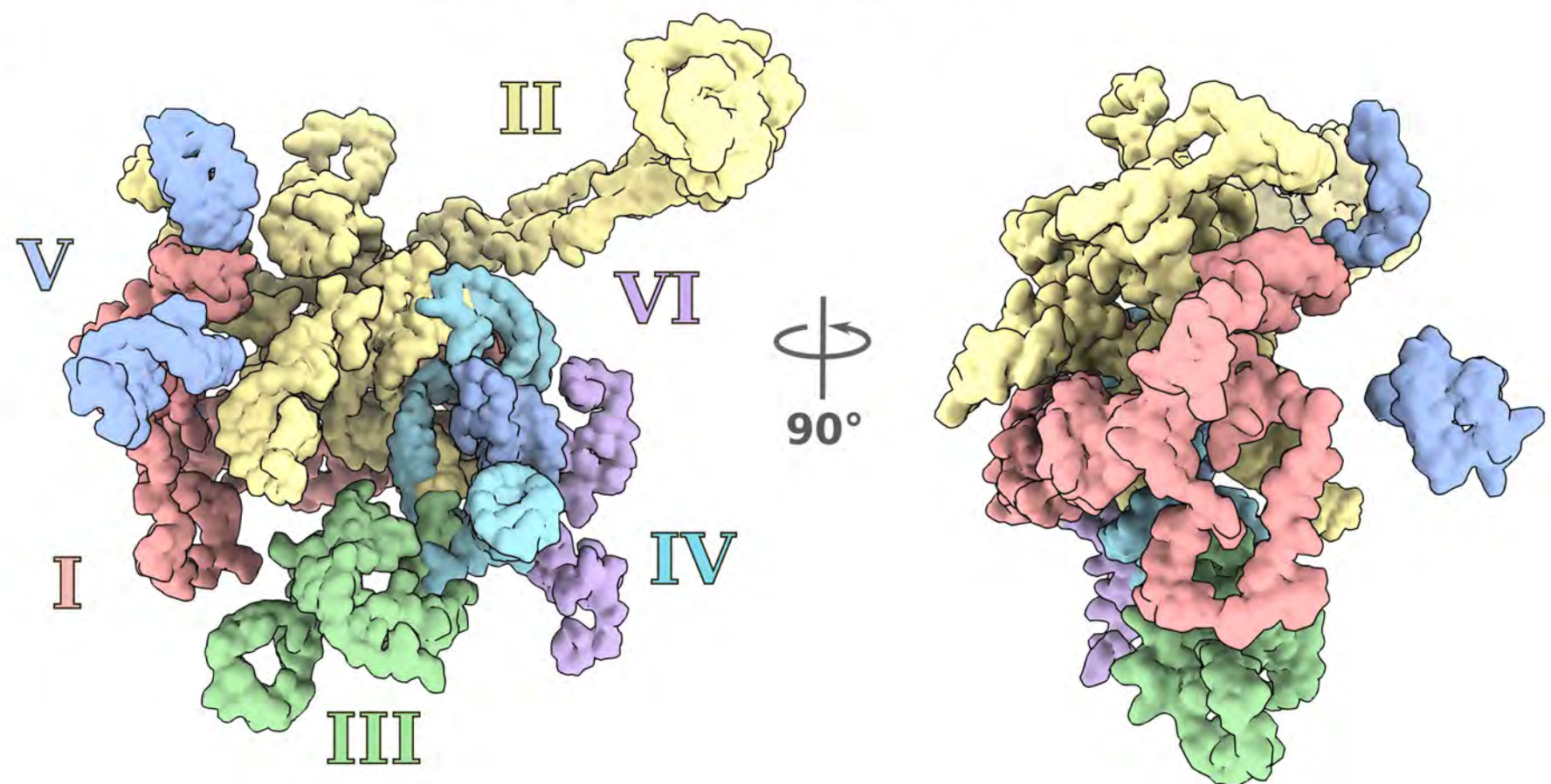


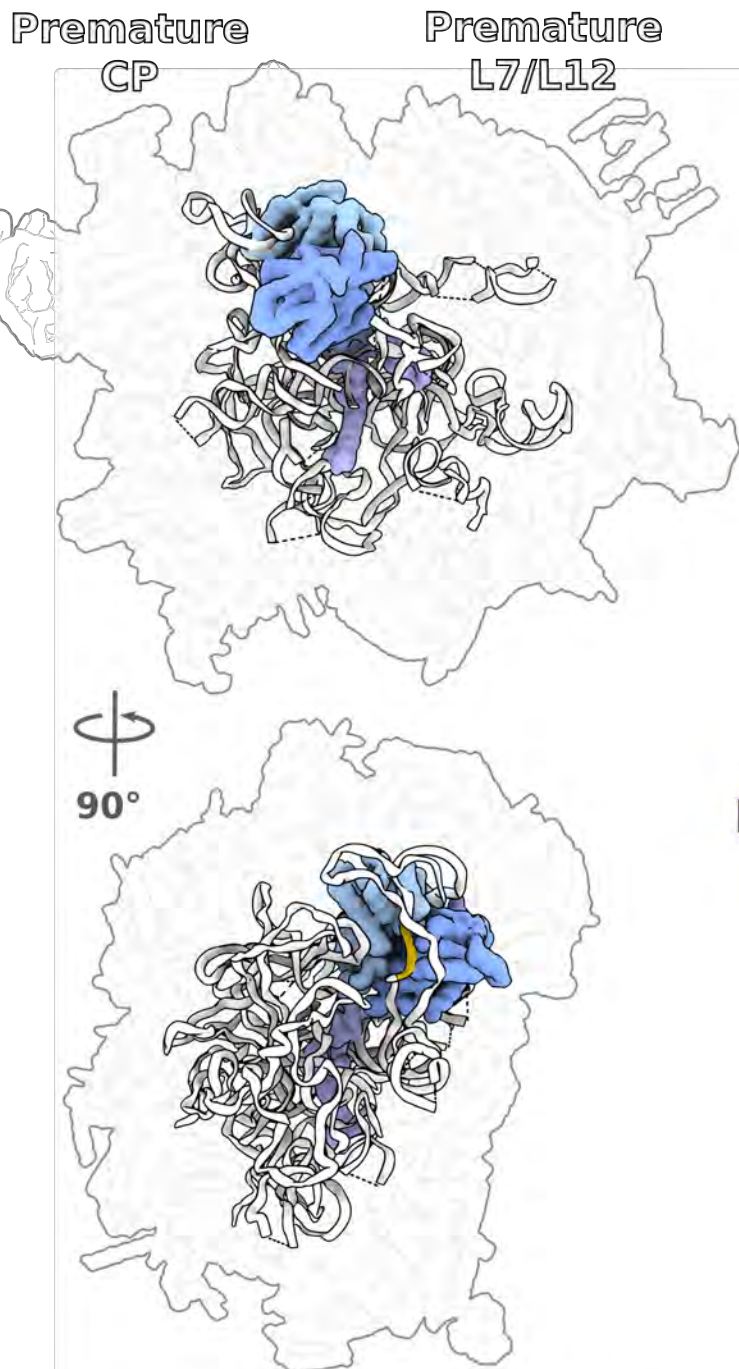
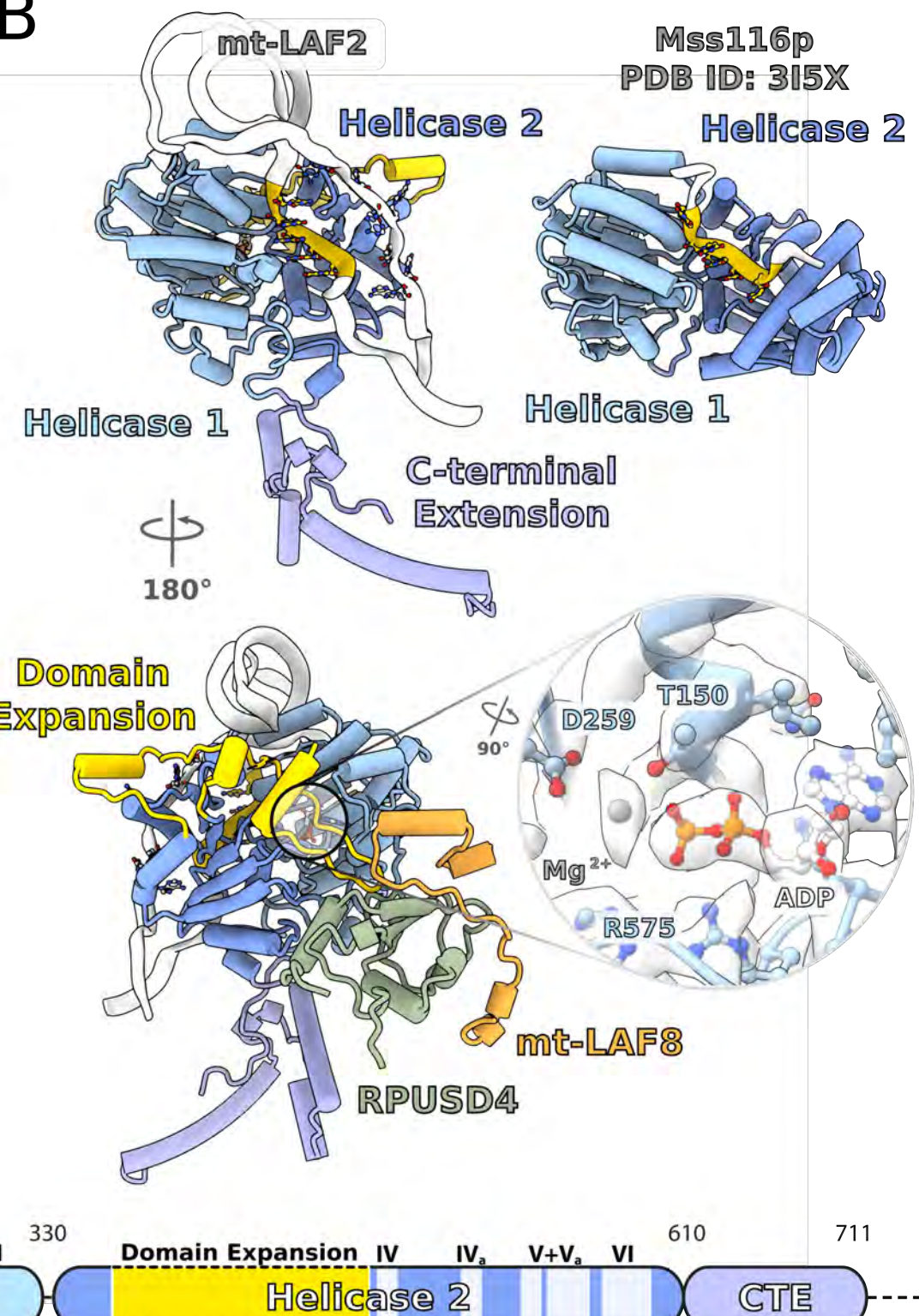
B



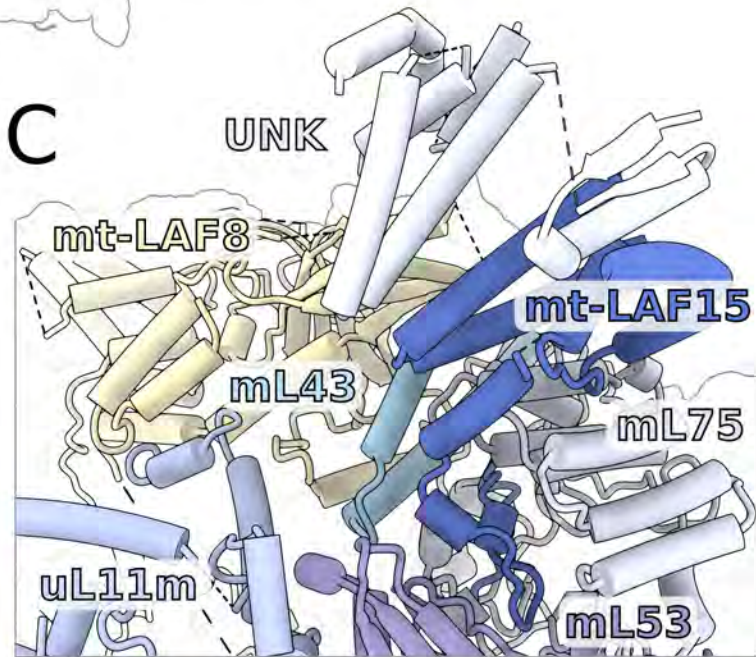
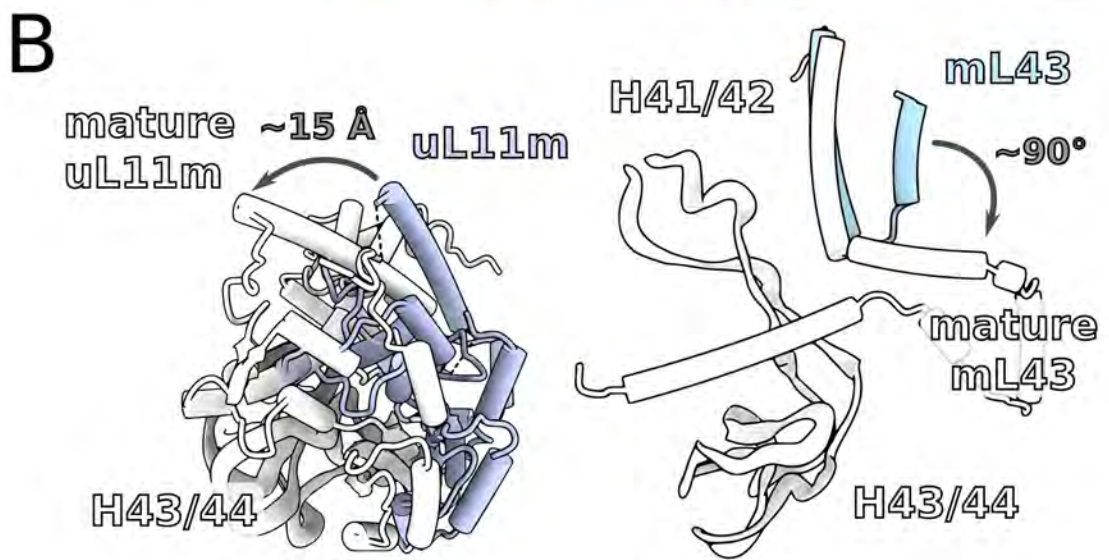
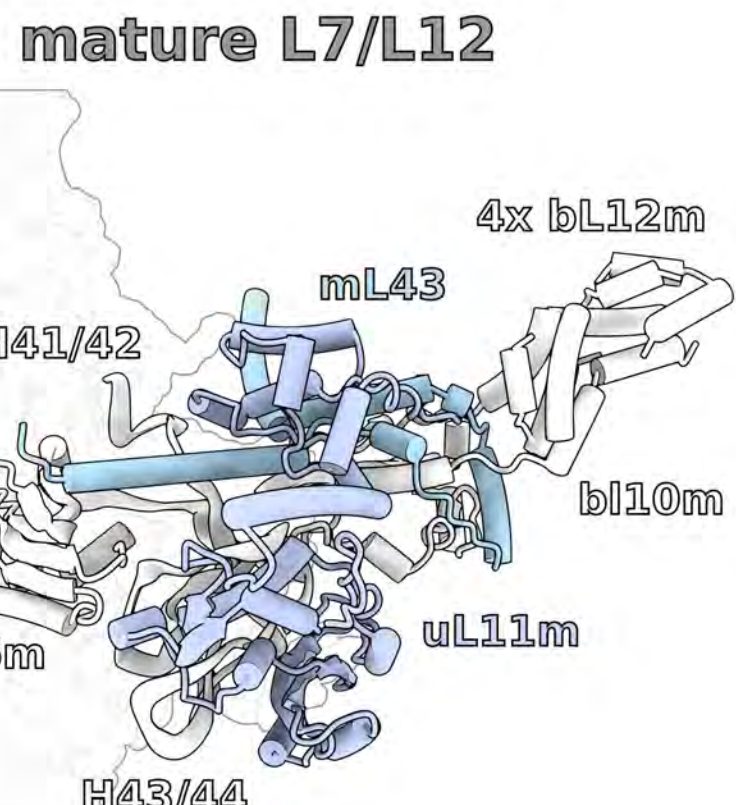
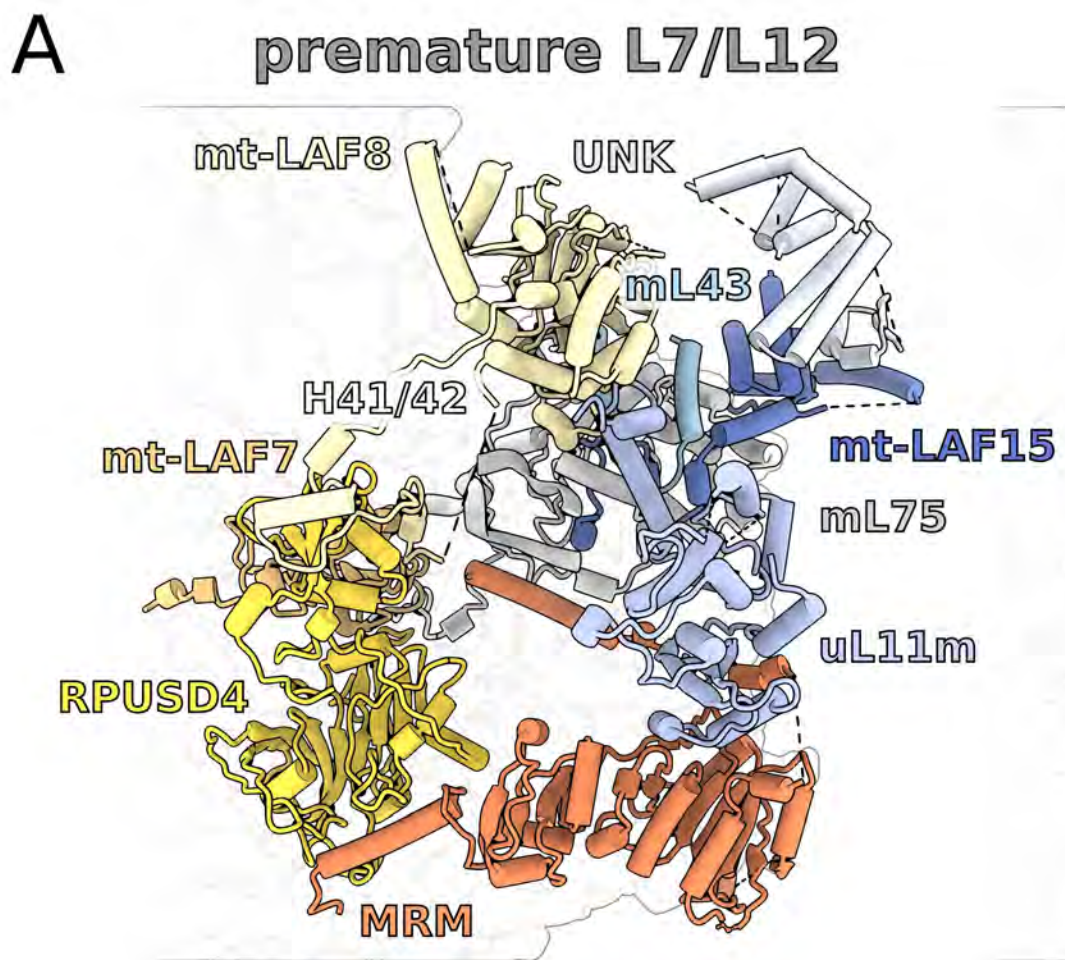
C

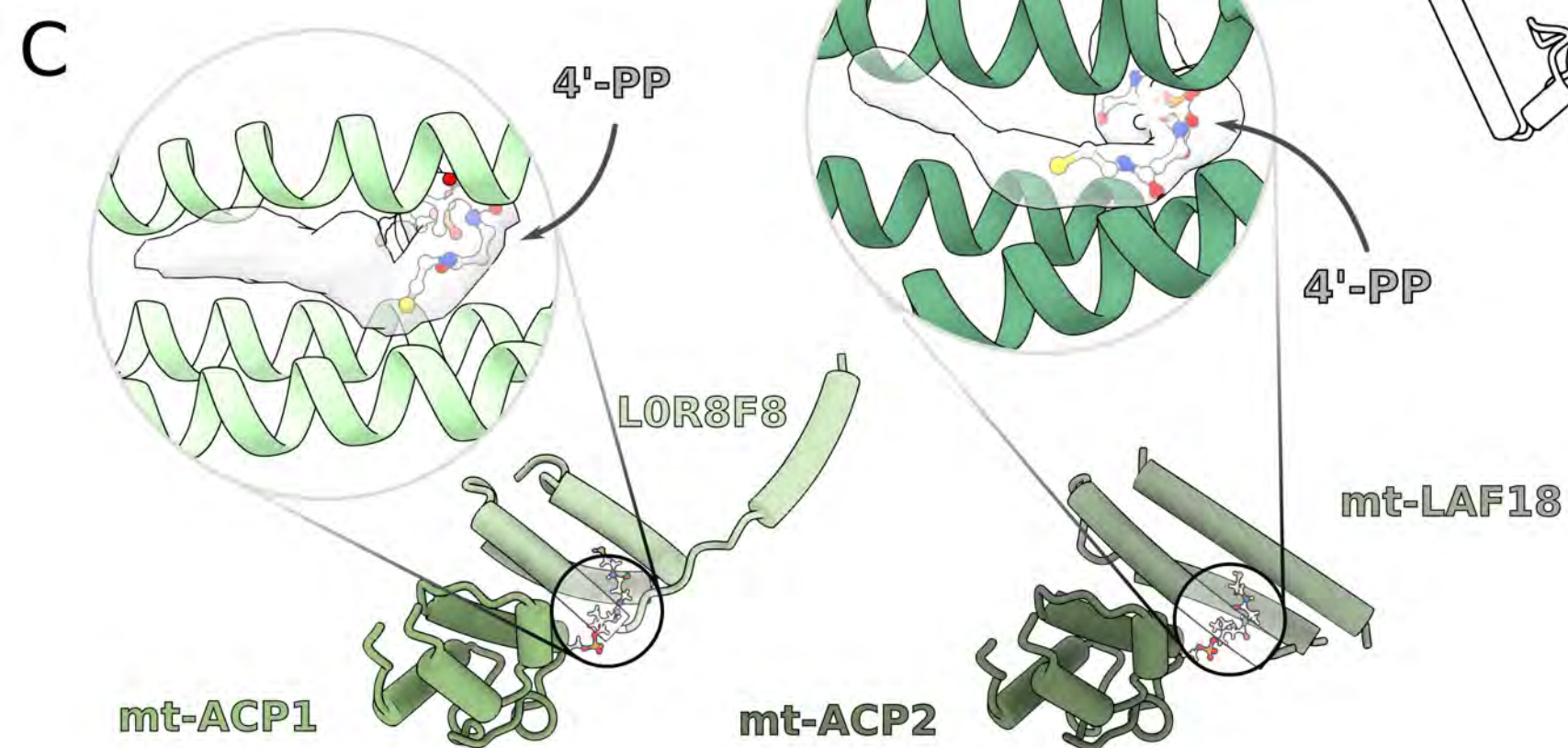
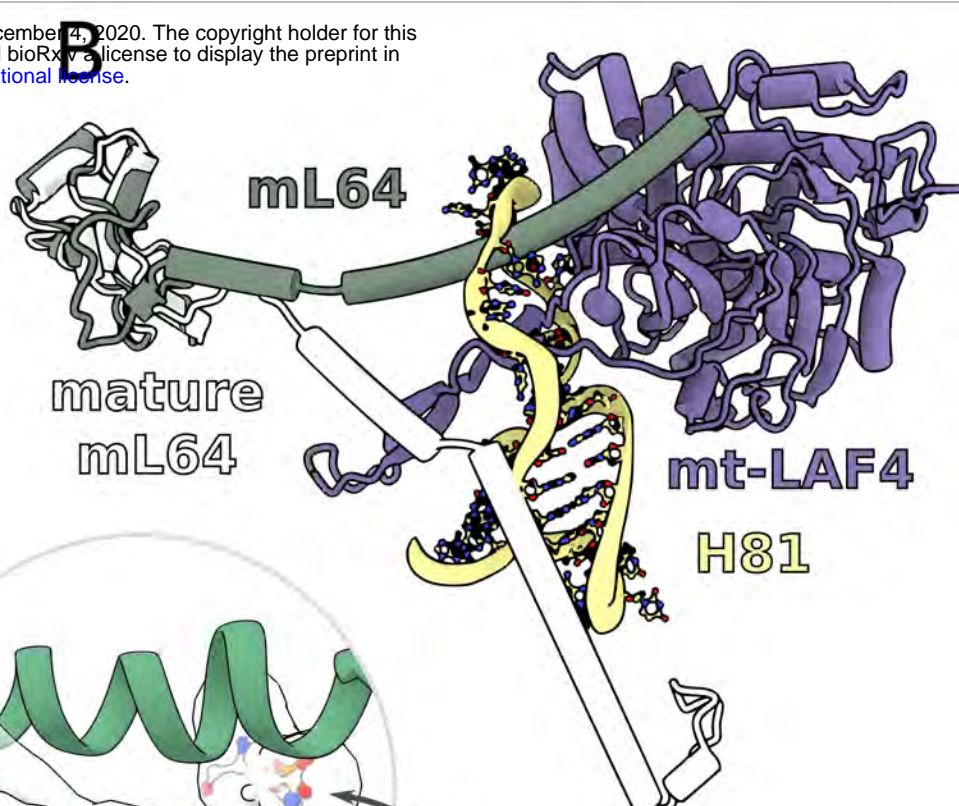
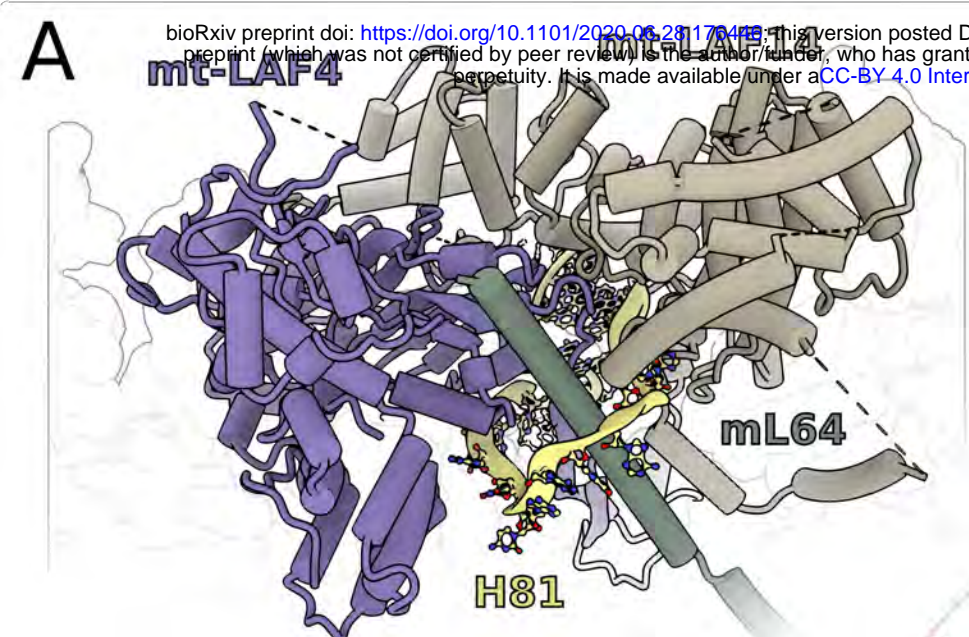


**A****B**

**A****B**

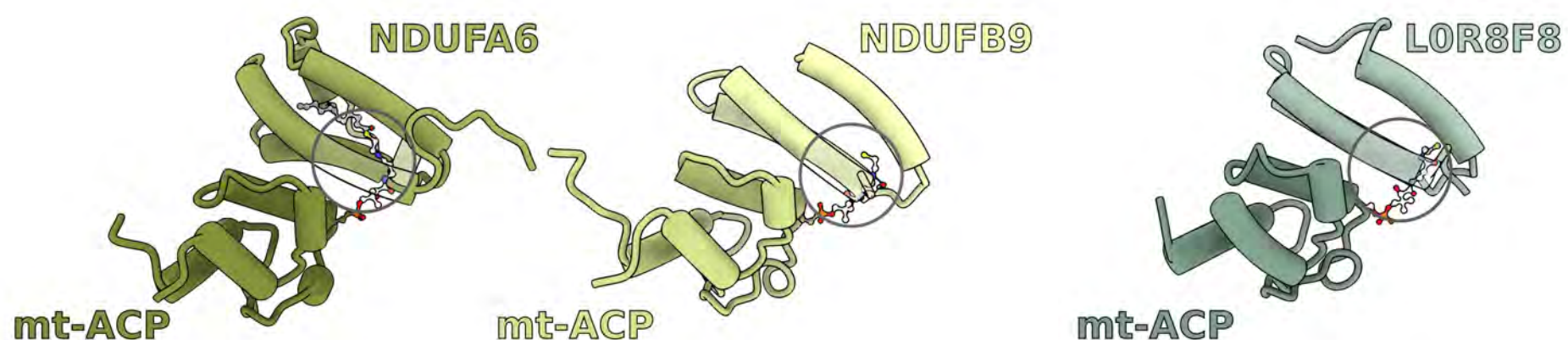
mt-LAF2   PSPIQ   HGEK   LAPTRELIAQ   TS   IMDPKIVLR   AVDEADGM   FATAF   IIFTRGI   HAALPAAVR   LCSTDVAARGLDLHVDFVNFD   YLSRAGRTARQG  
 consensus   PTPIQ   TGSKGT   LAPTRELAxQ   GG   VATPGRLLD   VLDEADRM   FSATF   IIFVNTK   HGxxxQxER   LIATDVV   ARGLDIPxVDFVINYD   YYHHRIGRTGRAG





---

*T.brucei* pre-mtLSU



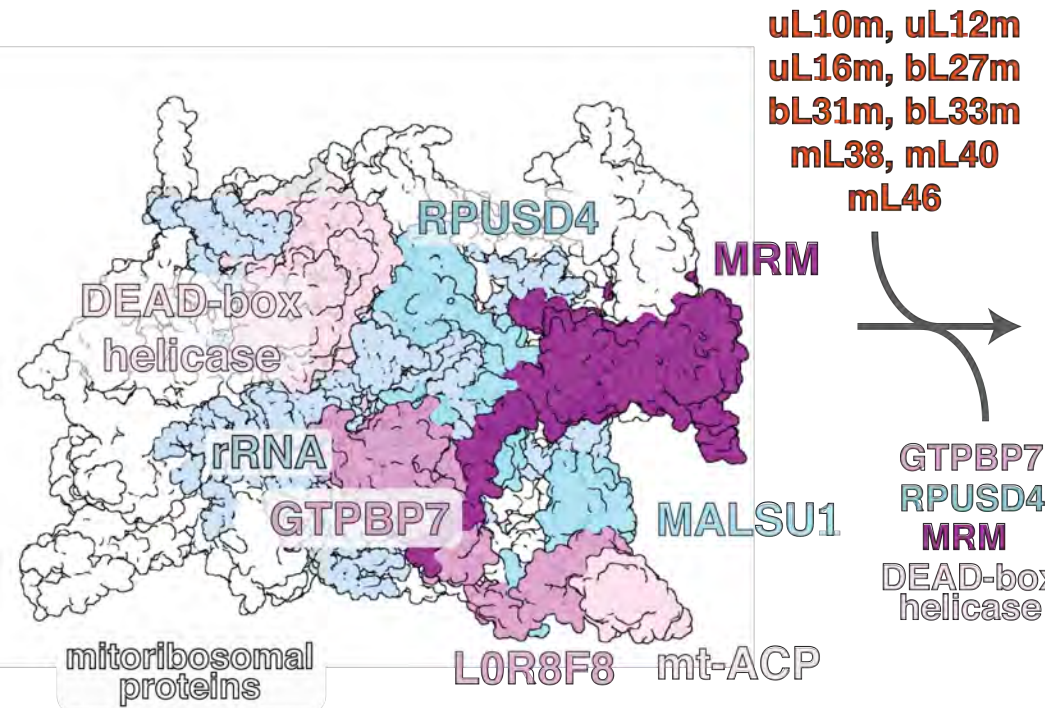
---

*O.aries* complex I

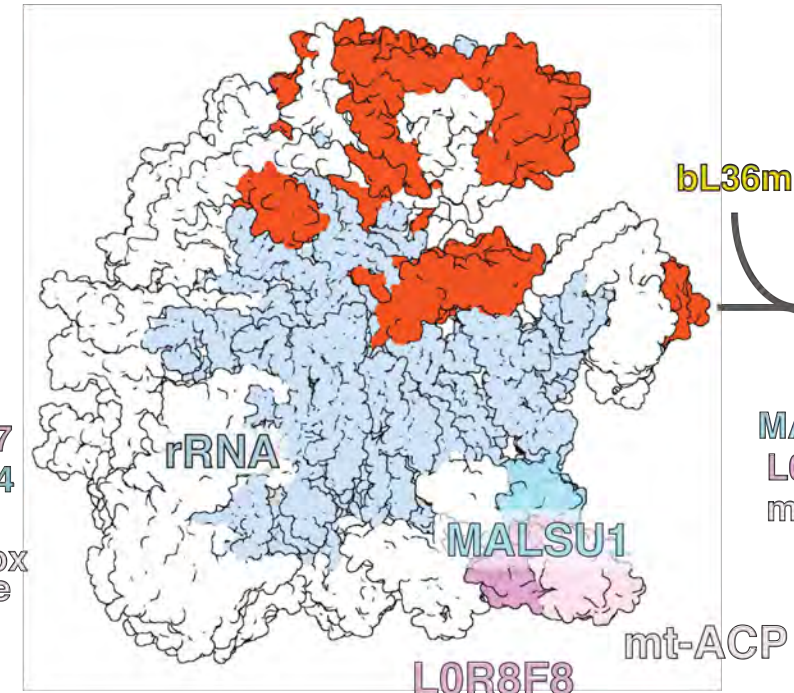
---

*H.sapiens* mtLSU

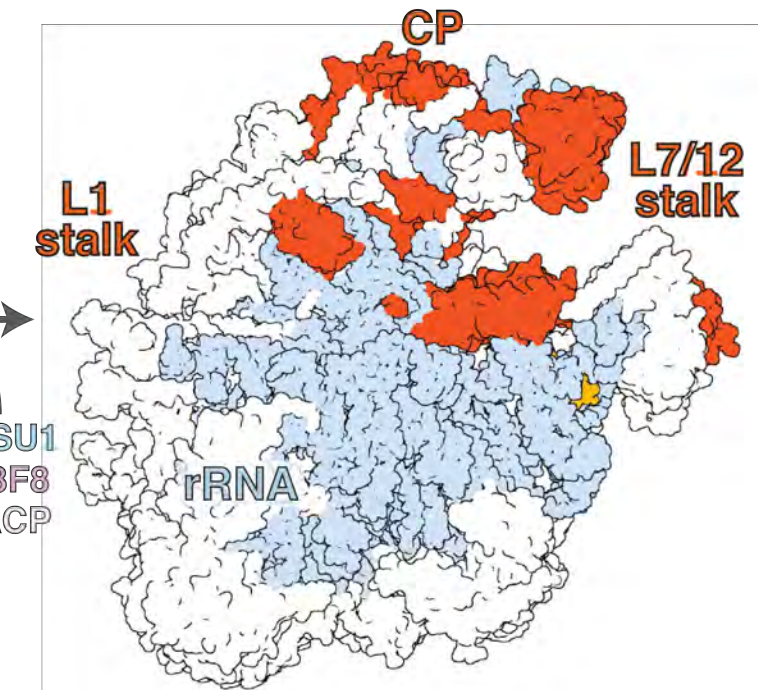
pre-mtLSU  
current work



late-stage intermediate  
PDB: 5OOL

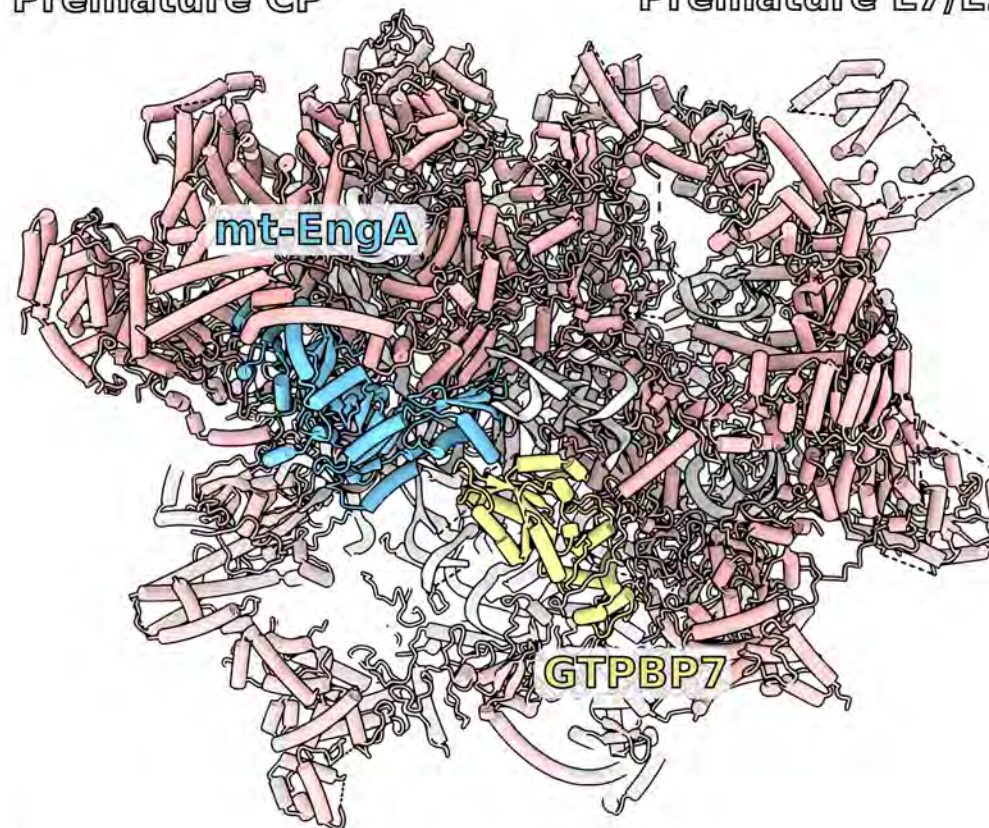
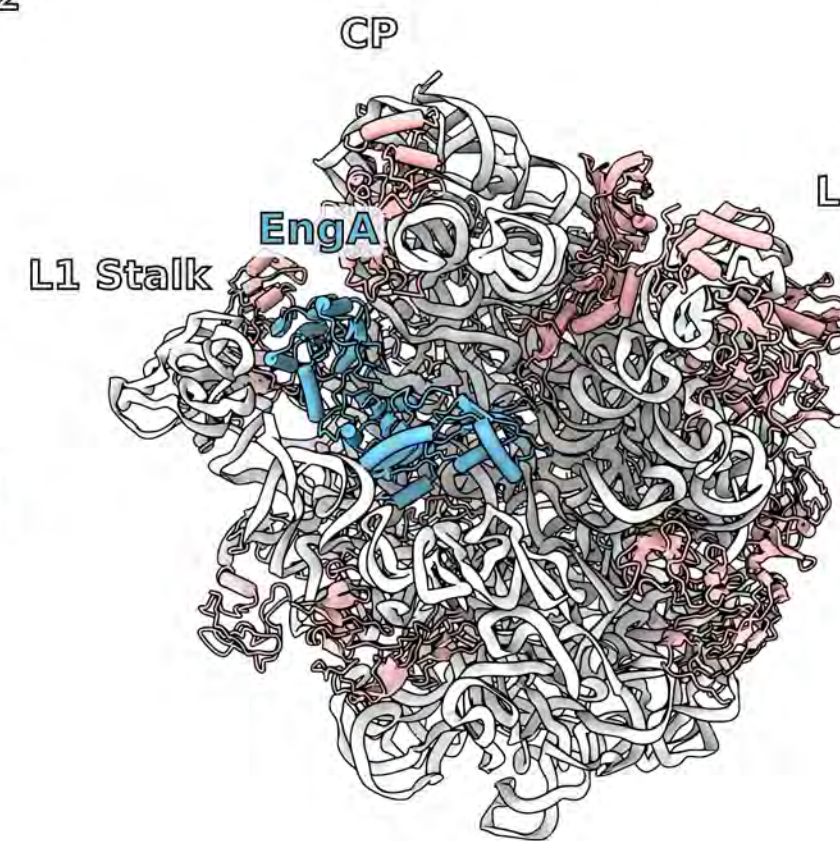
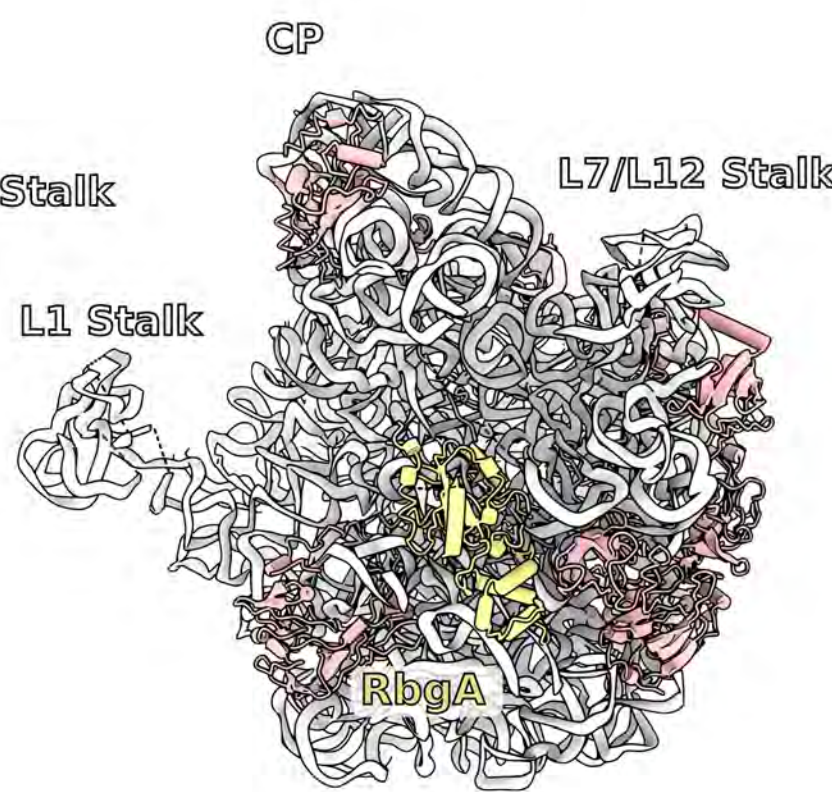
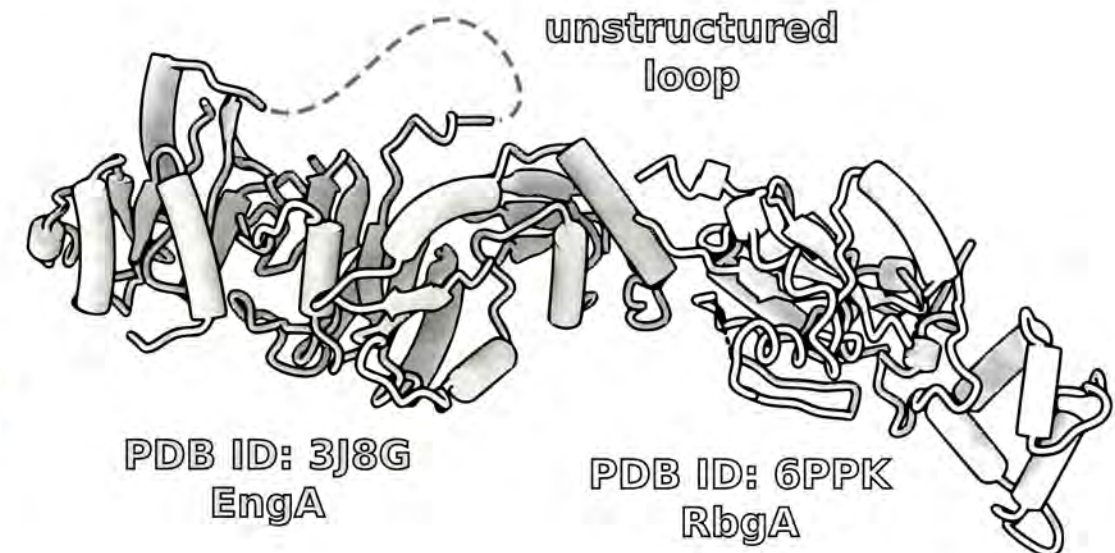
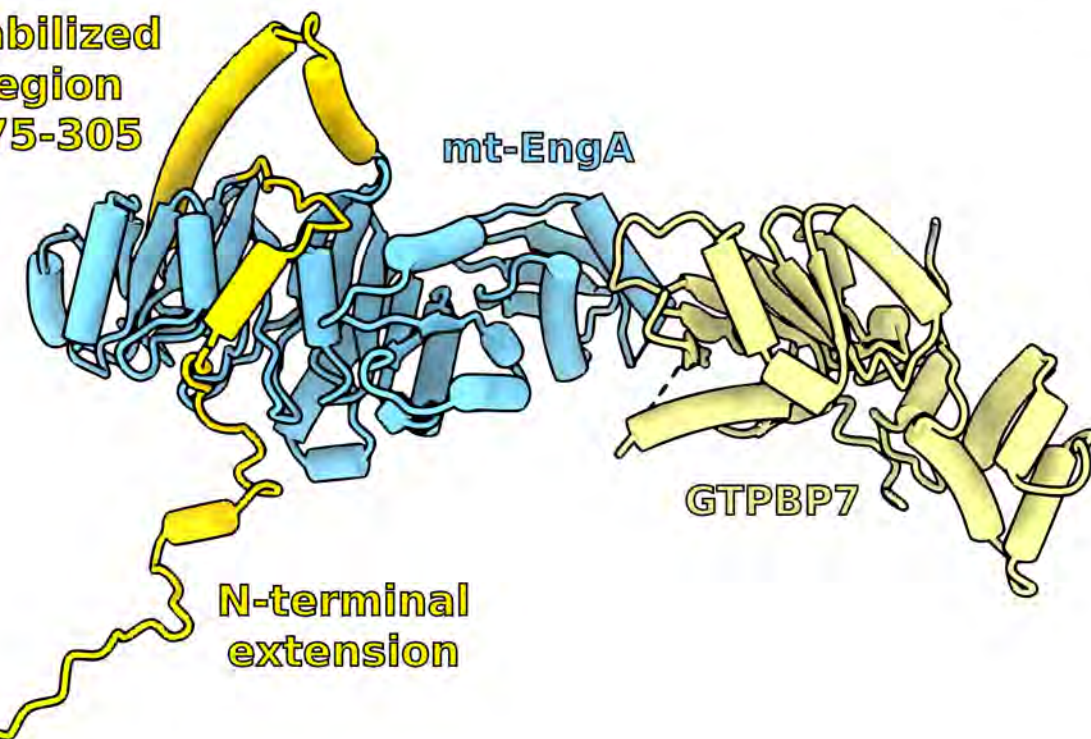


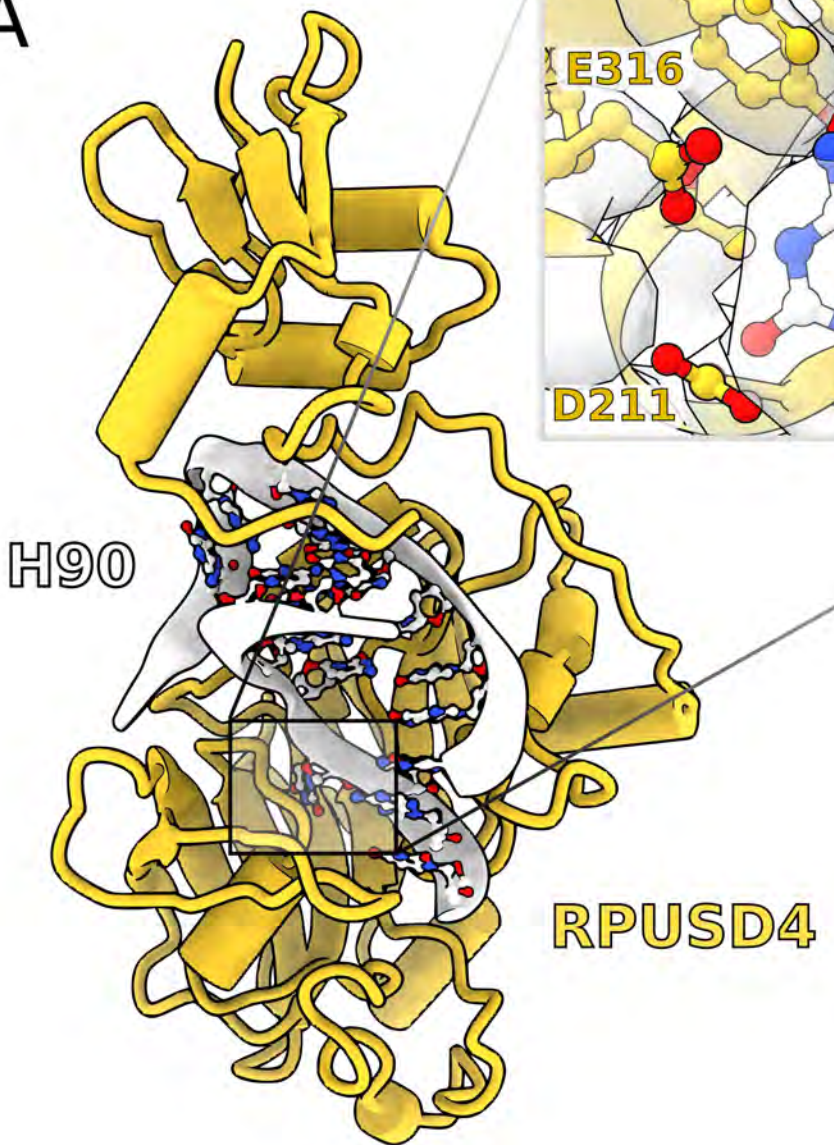
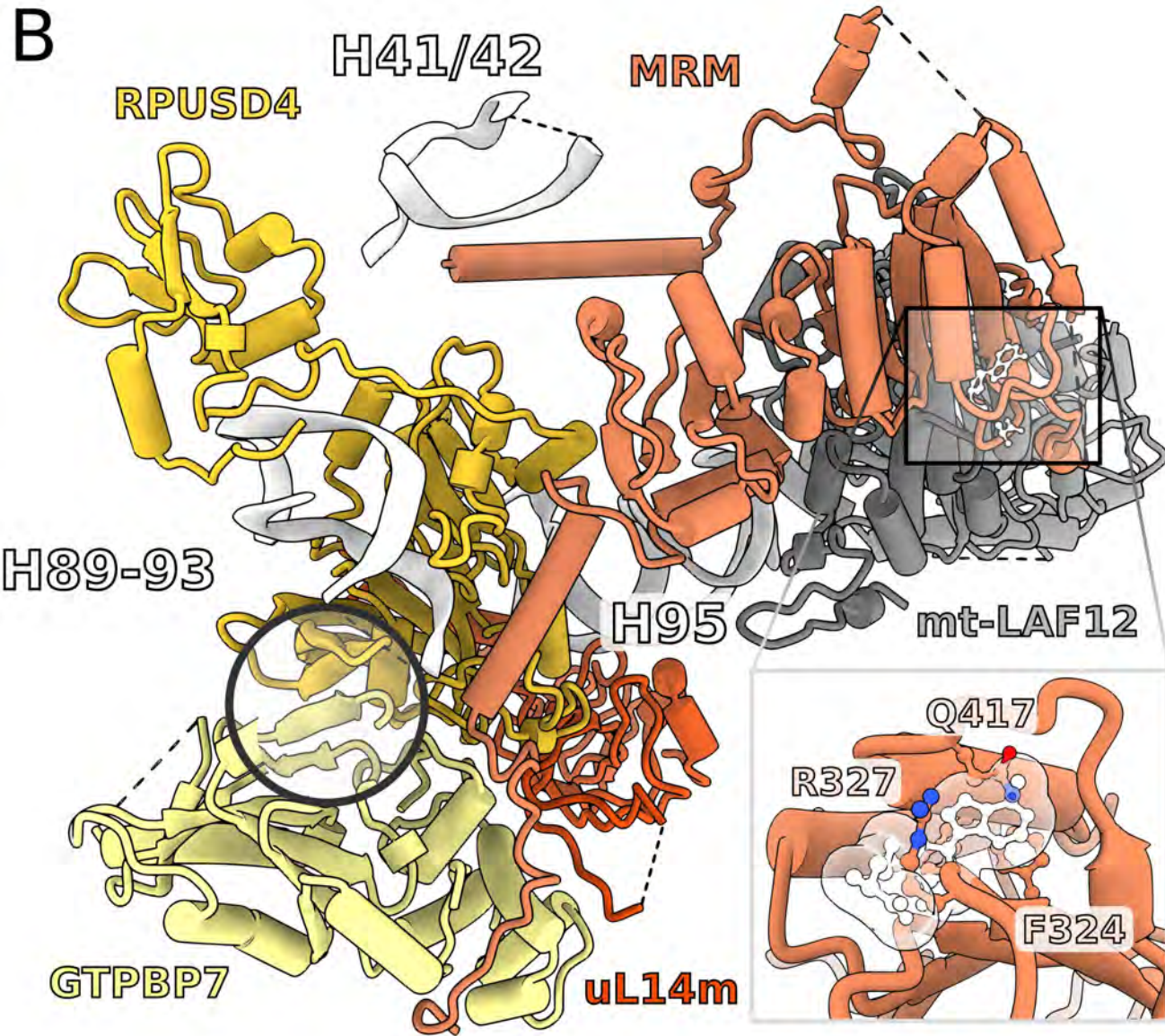
mature mtLSU  
PDB: 6ZSG

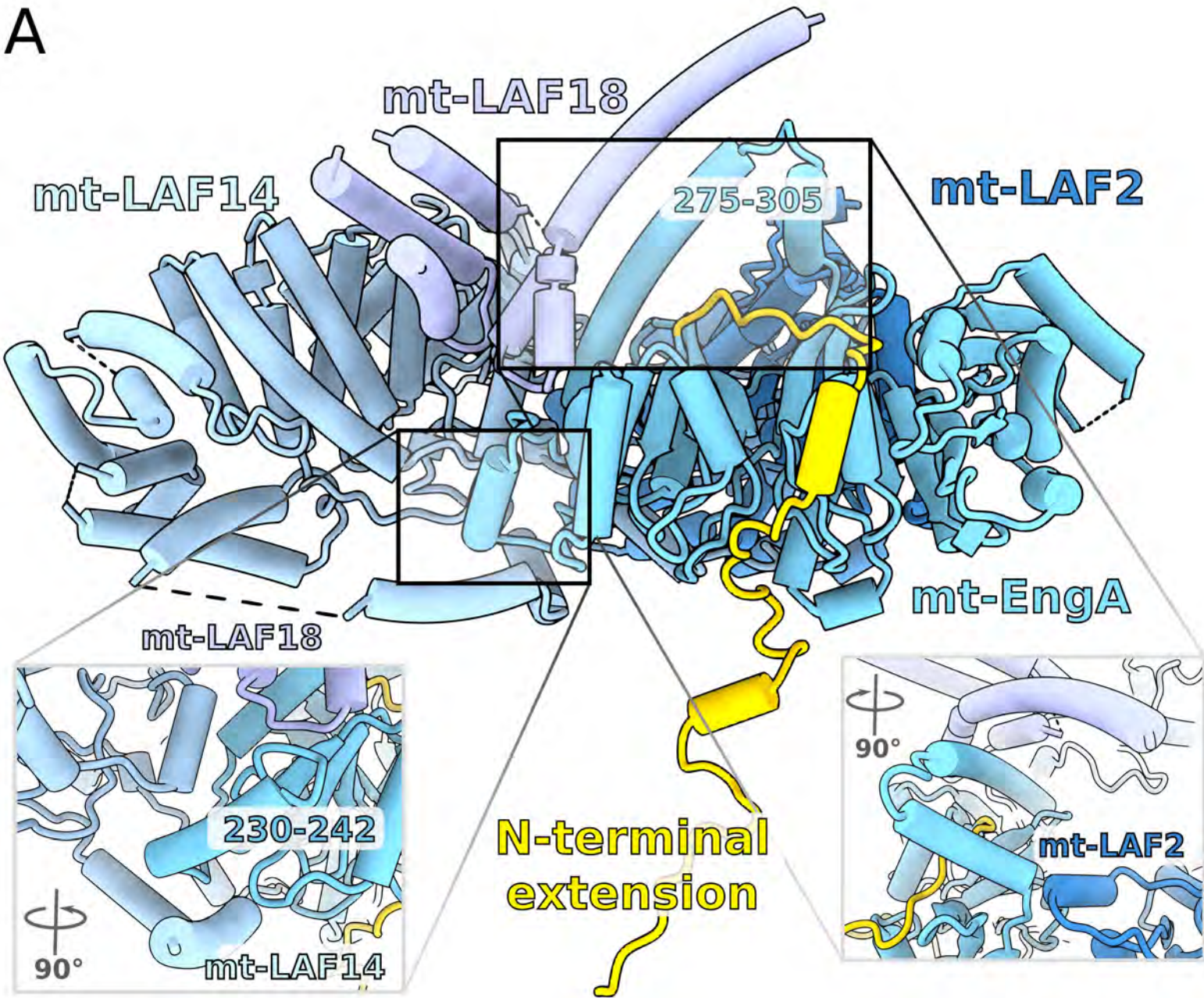


**A*****T. brucei* pre-mtLSU**

Premature CP

***E. coli* PDB ID: 3J8G*****B. subtilis* PDB ID: 6PPK****B**stabilized  
region  
275-305

**A****B**

**A****B**Position in *T. brucei*

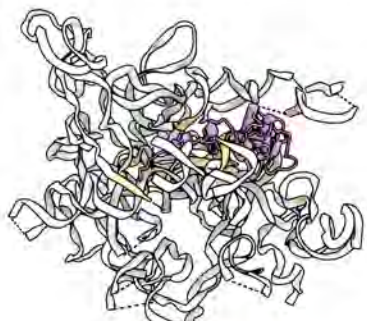
T.*brucei*  
L.*major*  
N.*gruberi*  
A.*castelanii*  
P.*falciparum*  
T.*thermophila*  
P.*parasitica*  
G.*theta*  
C.*reinhardtii*  
A.*thaliana*  
O.*sativa*  
T.*maritima*  
E.*coli*  
B.*subtilis*

5 MRRCIPASVLRRVLLQTRLVSTNTQTTPSGCATKIQNESPMNGSFNL  
15 MSCPIASARGLATSRGAGGSRGGGGSGRDRAQQTTRPHSQKSSSSSSAT  
25 MEHDDDDDDDDDEKGYDNDYDNHNDYHNDNYYGQNEFIQISSNKDYKQTLISNSQ  
35 MAAAIALRAALRRSRPAAAALLHHRPLPSSRSLP  
45 M

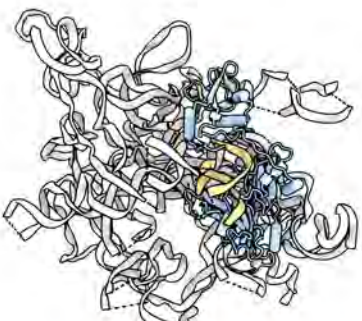
Position in *T. brucei*  
Identity

55 PRERQILGGLHADWR TQM KRS GSI LND ITP ALP DT KR TEE QRRR VAG WRP PVV KLL GD QRL RIAIVGRMNSGKSSLFN  
PRRTQI RGGLHFSW REEV KRS GSR LND I SPAMED TART D E QRRR VAG WTP PVV KTL GD HRL RVAIVGRMNSGKSSLFN  
65 RGAGGKG GGGK SNAARGPG AAAATKKRAPS GEASKAR PAEE EALG GVE S D TERY TMR RD PVL ALV GL PNC GKS TLF  
MTSKSS SAS GNM K TFD DN STS S YAG KVL KM VRS KKL N RVAIVGRMNSGKSSLFN  
75 EIN HNY IYD KEKR SS KTY I PNN I I QNN S NQ ED I Q I D D V QTE EN K K N K K K D V E L N I I R N L P L I S I I G R P N V G K S T I F N  
INL FRY QNK F LQ Q ASK Q T O I N K L A S V C N K G N K F S S L S L STAY K F C S F E N N D N F S R K D D Y T I S F V G R P N V G K S S L F N  
85 M L R S L V Q R S S R A S T G L L P V R V C F S S V V N E T E R S F L E D H P R L R I A L V G R I T N V G K S T I L F N  
MF I N V T V L N H L N K I K I N K D L I L D K I T H N F F T K K N Y L N S L K C D S T V Y N F N D Y K Q M R I P I I T V V G R S N V G K S T I L F N  
95 M F P E D E T I E G K E T R R K G K R L A K N T Q Q I P E H L I Q R V A I V G R P N V G K S A L F N  
PL P S L G R S S P L L S R F P G S A G F V Y S T V A D E S T A P V K P K G K A R K N P M K Q S R F D T K V D A A L L P T V I L V G R P N V G K S A L F N  
105 M A T V I I V G R P N V G K S T I L F N  
M V P V V A L V G R P N V G K S T I L F N  
115 M G K P V V A I V G R P N V G K S T I L F N  
125

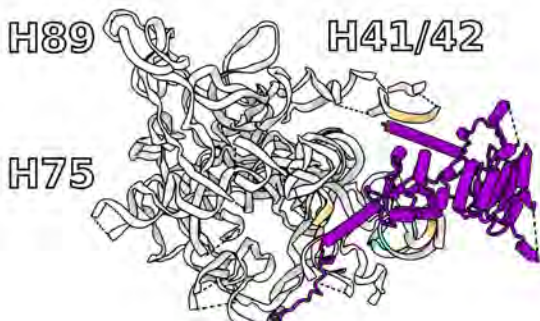
~200Å



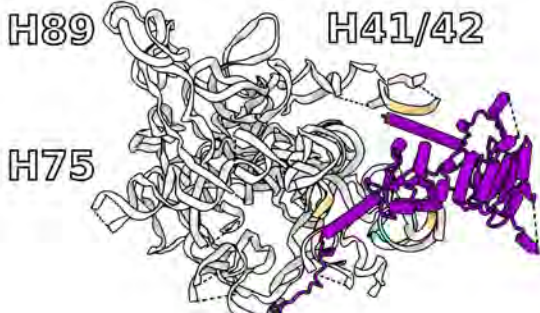
mt-LAF7



RPUSD4

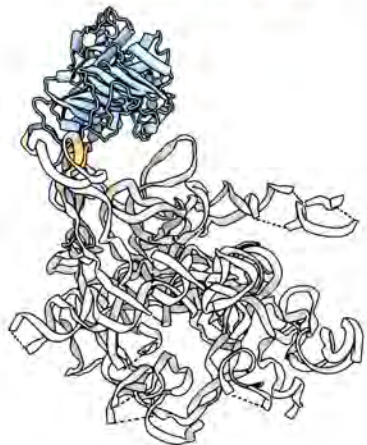


H75

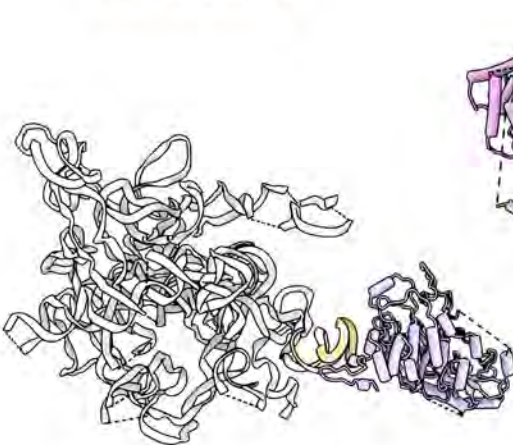


H41/42

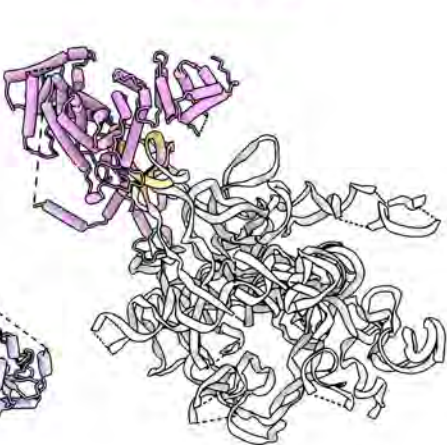
MRM



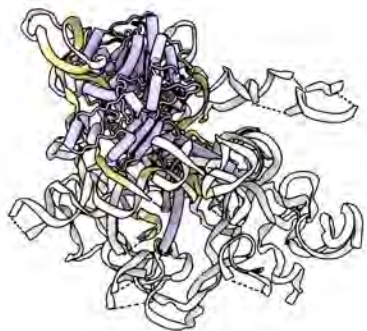
mt-LAF4



mt-LAF12



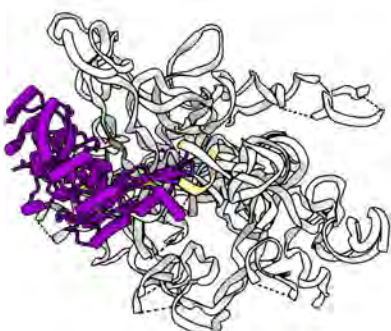
mt-LAF14



mt-LAF2



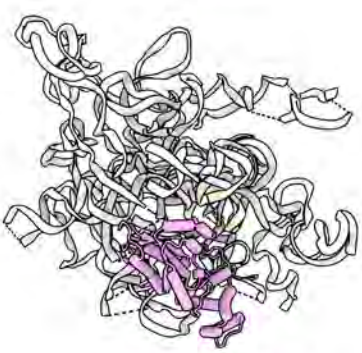
uL14m



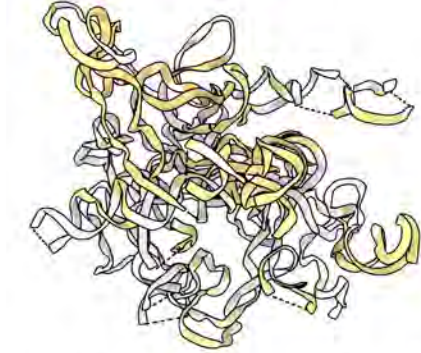
mt-EngA



MALSU1

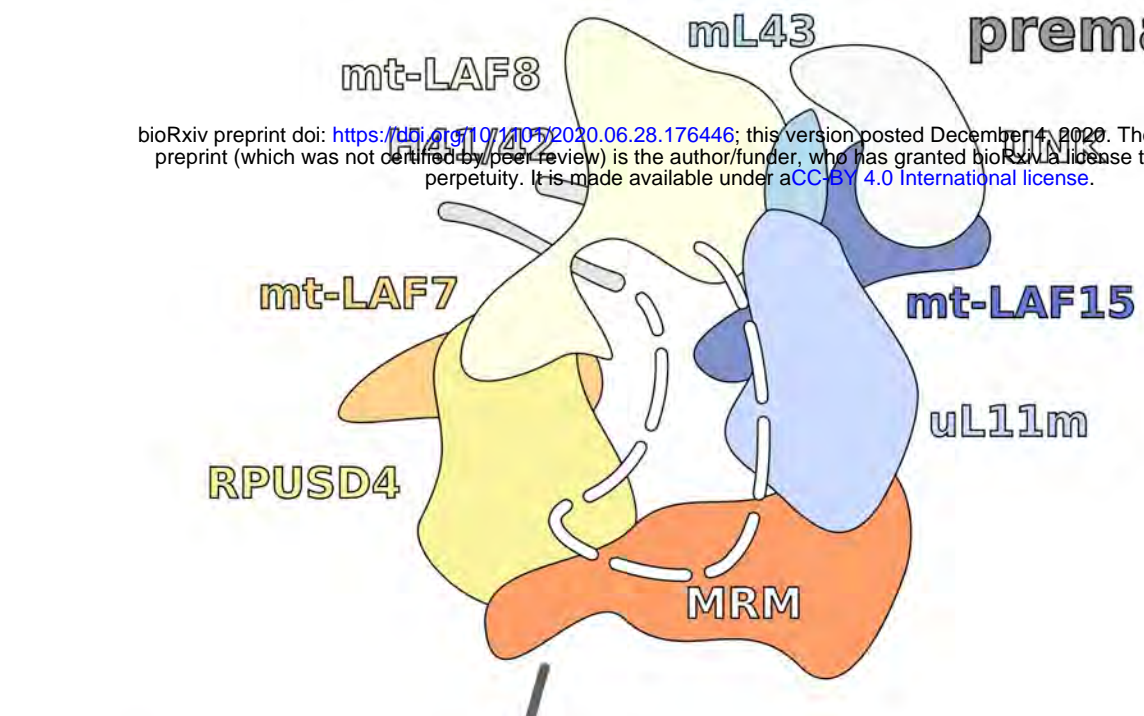


GTPBP7

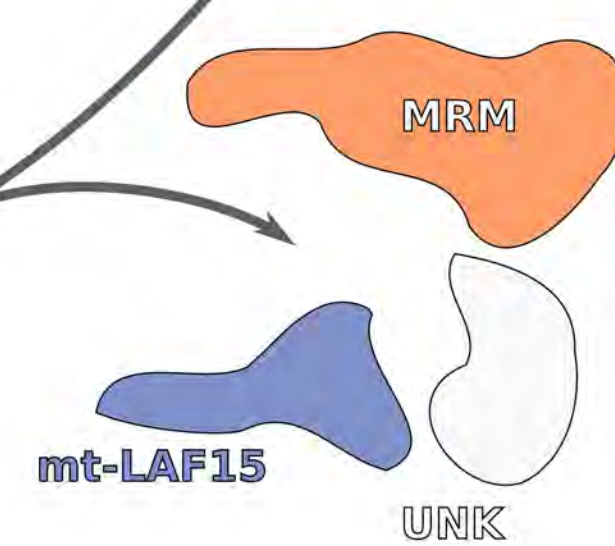
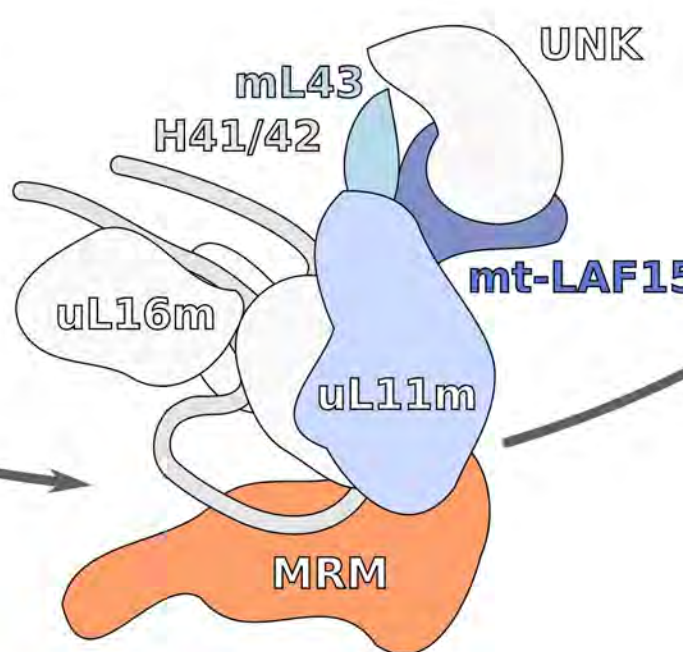
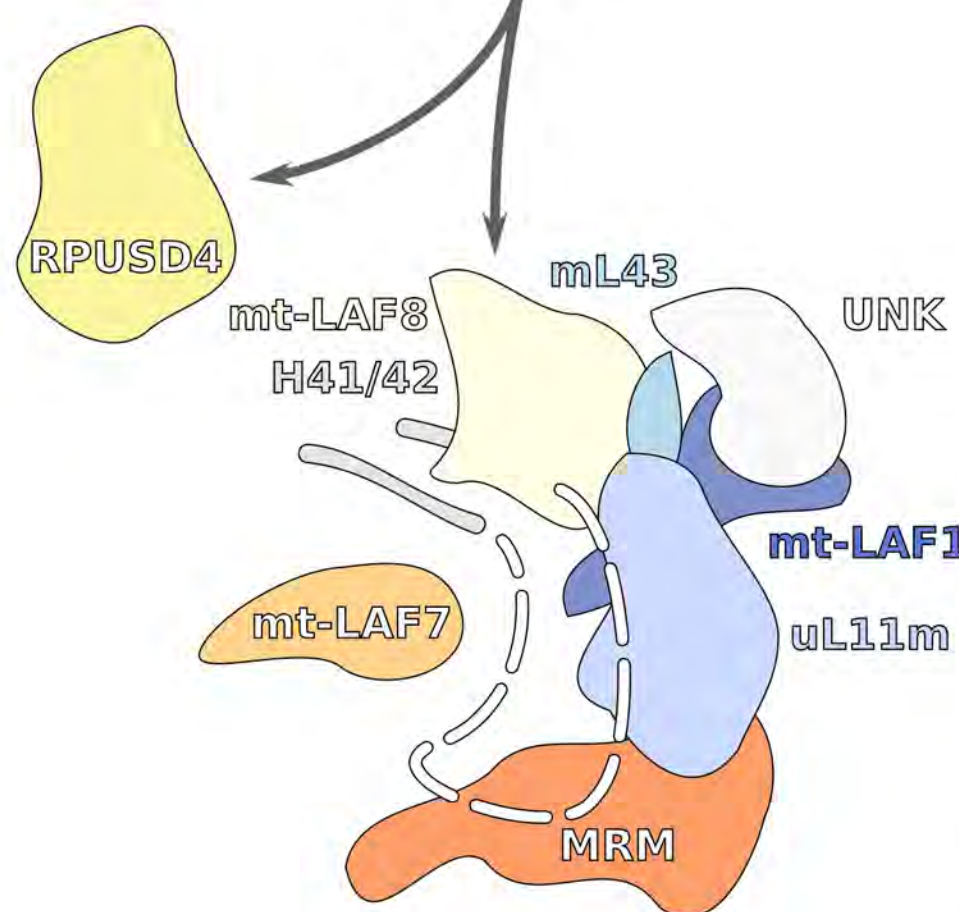
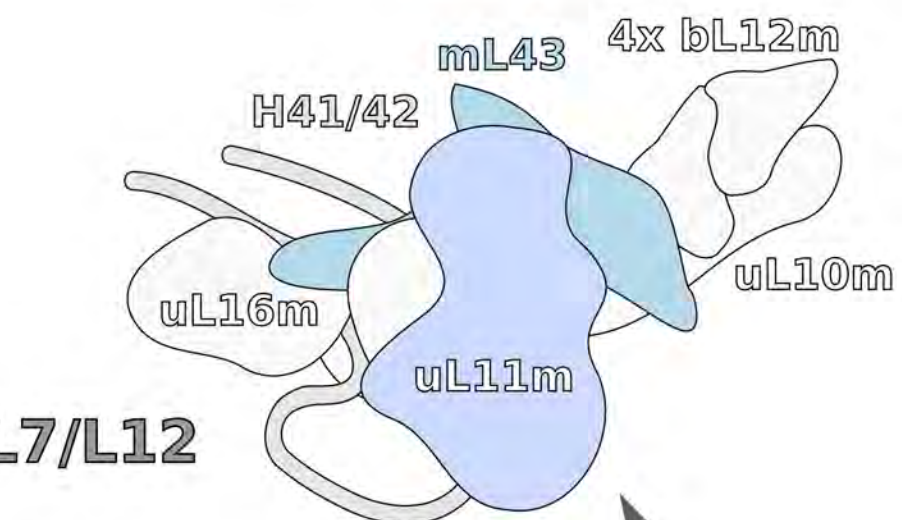


all TbLAF contacts

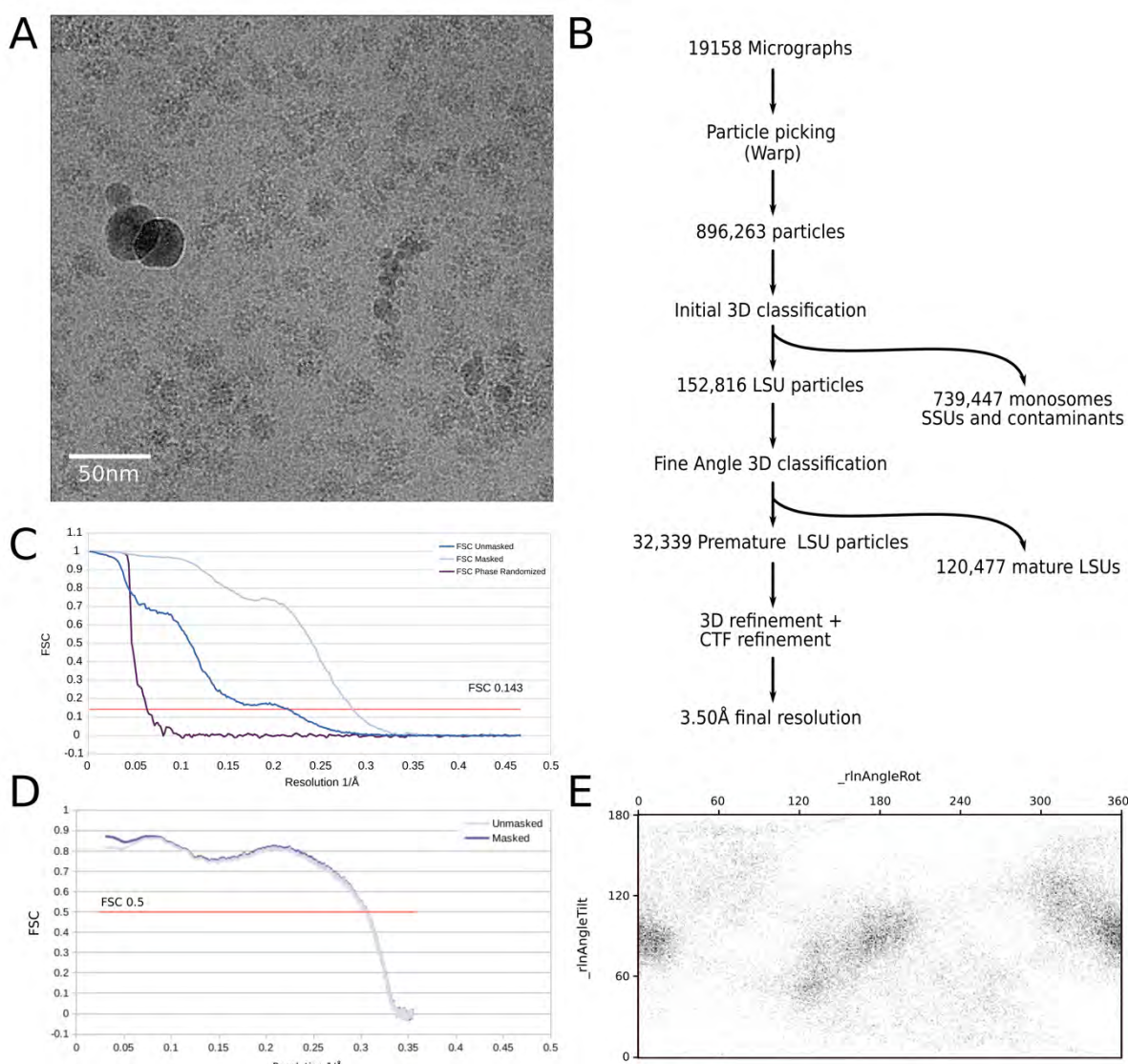
## premature L7/L12



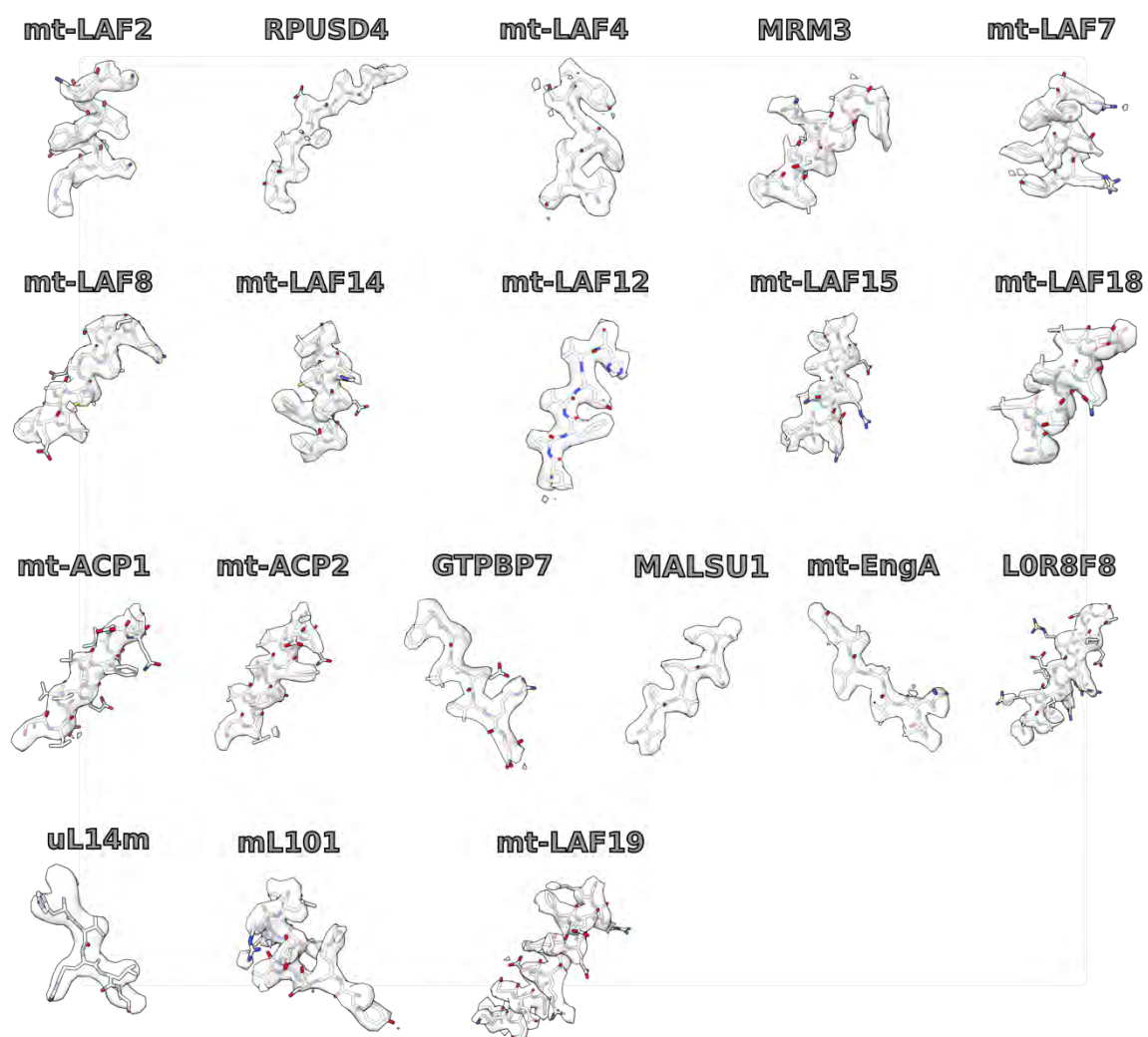
## mature L7/L12



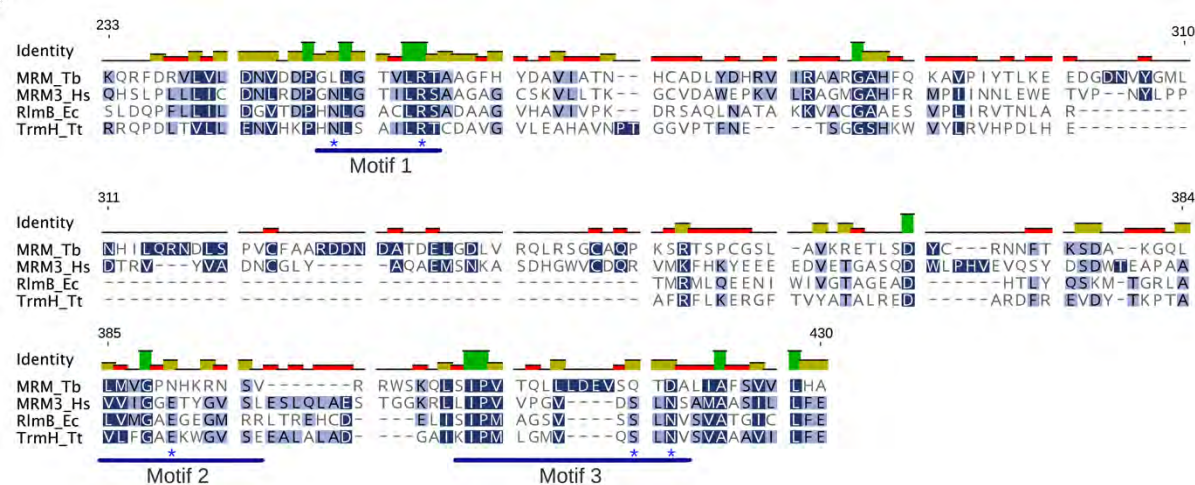
bioRxiv preprint doi: <https://doi.org/10.1101/2020.06.28.176446>; this version posted December 4, 2020. The copyright holder for this preprint (which was not certified by peer review) is the author/funder, who has granted bioRxiv a license to display the preprint in perpetuity. It is made available under aCC-BY 4.0 International license.



**Appendix Figure S1.** Cryo-EM data processing. **(A)** Representative micrograph. **(B)** Processing workflow. **(C)** Fourier shell correlation (FSC) curves. Resolution is estimated based on the 0.143 FSC cut-off criterion (red line). **(D)** Map to model FSC as calculated in PHENIX (Liebschner et al 2019). **(E)** Angular distribution plot for final reconstruction as calculated by RELION (Zivanov et al 2018).



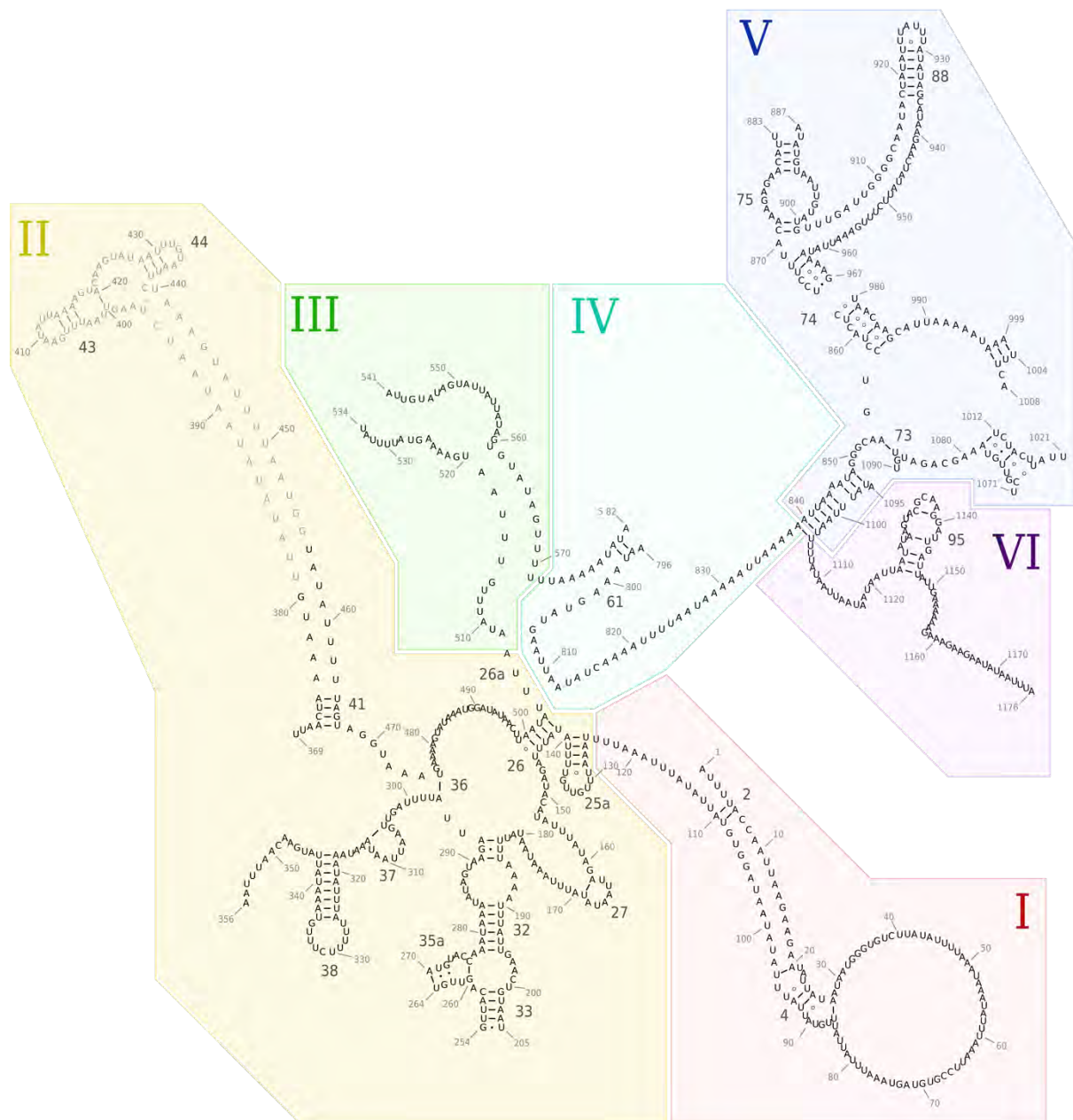
**Appendix Figure S2.** Examples of densities and models for individual assembly factors and newly identified proteins.



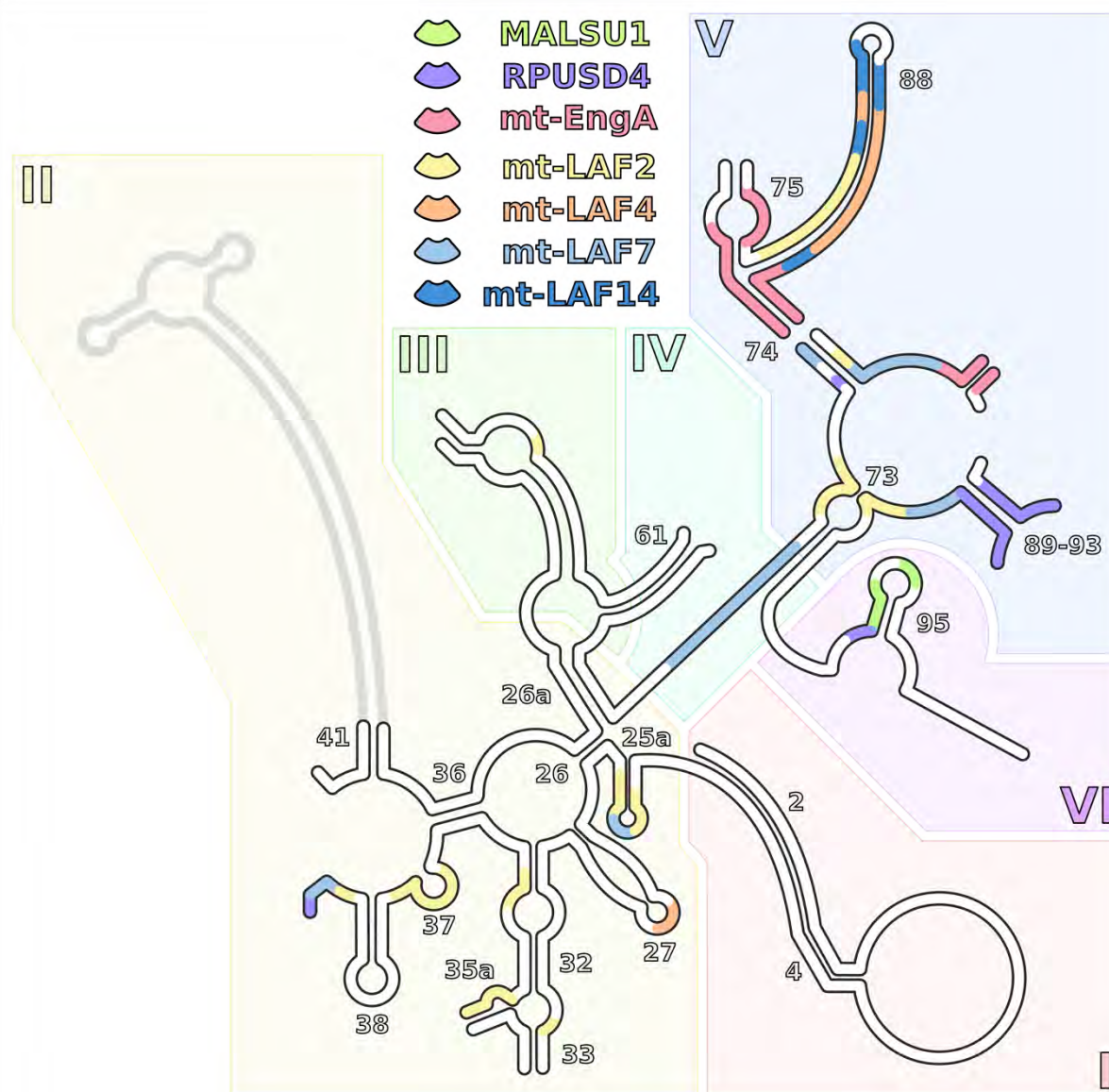
**Appendix Figure S3.** Sequence alignment of MRM homologs from representative bacterial and eukaryotic species (Hs *Homo sapiens*, Ec *E. coli*, Tt *Thermus thermophilus*). The asterisks mark residues important for catalysis.



**Appendix Figure S4.** Sequence alignment of EngA homologs from representative bacterial and eukaryotic species. The yellow, green, blue and orange horizontal bars mark the N-terminal extension, GTPase domain (GD) 1, GD2, and the KH domain, respectively. The white asterisks and crosses mark residues in *T. brucei* mt-EngA that coordinate GTP and interact with GTPBP7, respectively. The green, yellow, and red vertical bars above the alignment correspond to 100%, <100% and  $\geq 30\%$ , and <30% identities at the respective position.



**Appendix Figure S5.** Secondary structure rRNA diagram derived from the model and colored by domain. Unmodeled sections that appear in the mature mtLSU are shown in grey. Domains in Roman numerals.



**Appendix Figure S6.** Schematic representation of assembly factors' binding to rRNA mapped on the secondary structure diagram. The rRNA regions contacting individual assembly factors are represented by different colors. Bound regions of at least 3 nucleotides are shown. For regions where more than one factor is bound, only a factor with higher local binding is shown. Unbound rRNA is white, unmodeled rRNA is grey.

**Table S1. Cryo-EM data collection, refinement and validation statistics**

Consensus map	
<b>Data collection and processing</b>	
Magnification	130000x
Voltage (kV)	300
Electron exposure (e <sup>-</sup> /Å <sup>2</sup> )	35
Defocus range (μm)	-0.8 ~ -3.5
Pixel size (Å)	1.05
Symmetry imposed	C1
Initial particle images (no.)	896,263
Final particle images (no.)	32,339
Map resolution (Å)	3.50
FSC threshold 0.143	
Map resolution range (Å)	3.0~10
<b>Refinement</b>	
Map sharpening B factor (Å <sup>2</sup> )	-70
Model composition	
Non-hydrogen atoms	146831
Protein residues	17415
Ligands	10
B factors min/max/avg (Å <sup>2</sup> )	
Protein	17/172/68
Nucleotide	22/281/57
Ligand	35/194/61
R.m.s. deviations	
Bond lengths (Å)	0.002
Bond angles (°)	0.46
<b>Validation</b>	
MolProbity score	1.65
Clashscore	6.7
Poor rotamers (%)	0.35
Ramachandran plot	
Favored (%)	95.6
Allowed (%)	4.10
Disallowed (%)	0.03

**Table S2. Summary of pre-mtLSU components**

Alias	Chain ID	TriTrypDB Gene ID (Lister strain 427)	TriTrypDB Gene ID (reference strain TREU927)	Uniprot ID (reference strain TREU927)	Full size	Modeled residues	Comment
<b>12S rRNA</b>	AA	rRNA	rRNA	N/A	1176	1-205, 254-264, 270-356, 369-380, 404-413, 445-450, 456-534, 541-582, 591-594, 796-883, 887-967, 980-999, 1004-1008, 1012-1021, 1071-1090, 1095-1176	
<b>uL3m</b>	AE	Tb427.03.5610	Tb927.3.5610	Q580R4	473	38-265, 272-404	
<b>uL4m</b>	AF	Tb427tmp.02.3810	Tb927.11.6000	Q385G8	351	18-459	
<b>bL9m</b>	AI	Tb427.05.3410	Tb927.5.3410	Q57UC5	263	9-220	
<b>uL11m</b>	AK	Tb427.02.4740	Tb927.2.4740	N/A	342	26-200, 207-235, 239-306	239-306 built as UNK
<b>uL13m</b>	AN	Tb427.04.1070	Tb927.4.1070	Q580D5	202	10-180	
<b>uL14m</b>	XG	Tb427.04.930	Tb927.4.930	Q580C1	217	20-107, 114-189	
<b>uL15m</b>	AP	Tb427.05.3980	Tb927.5.3980	Q57U68	374	10-136, 150-322, 354-363	
<b>bL17m</b>	AR	Tb427.08.5860	Tb927.8.5860	Q57YI7	301	11-266	
<b>bL19m</b>	AT	Tb427.01.1210	Tb927.1.1210	Q4GZ98	144	2-139	
<b>bL20m</b>	AU	Tb427tmp.01.1930	Tb927.11.10170	Q383R2	213	10-140, 162-205	
<b>bL21m</b>	AV	Tb427.07.4140	Tb927.7.4140	Q57UP4	188	6-185	
<b>uL22m</b>	AW	Tb427.07.2760	Tb927.7.2760	Q57Y86	278	2-278	
<b>uL23m</b>	AX	Tb427tmp.03.0260	Tb927.11.870	Q387G3	246	64-228	
<b>uL24m</b>	AY	Tb427.03.1710	Tb927.3.1710	Q57ZE0	378	1-311, 318-340	
<b>bL28m</b>	A1	Tb427.06.4040	Tb927.6.4040	Q586A2	241	10-226	
<b>uL29m</b>	A2	Tb427tmp.160.5240	Tb927.9.7170	Q38EM7	471	9-233, 248-471	
<b>uL30m</b>	A3	Tb427tmp.211.0230	Tb927.9.8290	Q38ED8	218	51-200	
<b>bL32m</b>	A5	Tb427.04.2330	Tb927.4.2330	Q584F4	80	26-80	2Fe-2S cluster binding
<b>bL35m</b>	A8	Tb427.10.1870	Tb927.10.1870	Q38C55	181	40-181	

<b>mL41</b>	Ae	Tb427tmp.01.1600	Tb927.11.9830	Q383U6	197	47-161	
<b>mL42</b>	Af	Tb427tmp.01.1840	Tb927.11.10080	Q383S1	189	41-173	
<b>mL43</b>	Ag	Tb427.04.4600	Tb927.4.4600	Q583E5	260	2-186	
<b>mL49</b>	Al	Tb427.05.3110	Tb927.5.3110	Q57Z82	218	37-101, 114-218	
<b>mL52</b>	Ao	Tb427tmp.02.2250	Tb927.11.4650	Q385V2	152	19-151	
<b>mL53</b>	Ap	Tb427.07.2990	Tb927.7.2990	N/A	309	16-303	
<b>mL63</b>	At	Tb427.07.7010	Tb927.7.7010	Q57XS1	154	10-154	
<b>mL64</b>	Av	Tb427tmp.01.3500	Tb927.11.11630	Q383B7	242	27-222	NAD binding
<b>mL67</b>	BA	Tb427tmp.55.0016	Tb927.11.1630	Q386Z1	831	27-83, 130-328, 335-542, 562-824	
<b>mL68</b>	BB	Tb427.10.600	Tb927.10.600	Q38CI0	541	62-258, 264-294, 304-341, 346-450	264-294, 304-341 built as UNK
<b>mL70</b>	BD	Tb427.06.4200	Tb927.6.4200	Q586Y7	547	105-521	
<b>mL71</b>	BE	Tb427.07.3460	Tb927.7.3460	Q57WG1	449	11-190, 228-448	
<b>mL72</b>	BF	Tb427.06.3930	Tb927.6.3930	Q585Z1	426	26-62, 118-421	
<b>mL74</b>	BH	Tb427.10.7380	Tb927.10.7380	Q38AM5	349	89-314	
<b>mL75</b>	BI	Tb427.10.380	Tb927.10.380	Q38CK0	342	20-342	
<b>mL76</b>	BJ	Tb427tmp.01.2340	Tb927.11.10570	Q383M2	333	173-333	
<b>mL77</b>	BK	Tb427.06.2480	Tb927.6.2480	Q584Q8	386	84-156, 188-233, 254-269, 280-386	254-259 built as UNK
<b>mL78</b>	BL	Tb427.10.11050	Tb927.10.11050	Q389N4	312	31-130, 141-197, 216-265, 281-306	
<b>mL80</b>	BN	Tb427.06.1440	Tb927.6.1440	Q585A3	302	53-266	
<b>mL81</b>	BO	Tb427tmp.02.3230	Tb927.11.5530	Q385L5	262	36-193, 210-262	
<b>mL83</b>	BQ	Tb427.07.3430	Tb927.7.3430	Q57WF8	231	16-200	
<b>mL84</b>	BR	Tb427.06.4080	Tb927.6.4080	Q586A6	205	11-205	
<b>mL85</b>	BS	Tb427tmp.160.2250	Tb927.9.3640	Q38FG8	198	20-163	

<b>mL86</b>	BT	Tb427.05.4120	Tb927.5.4120	Q57Z37	191	10-176	
<b>mL87</b>	BU	Tb427tmp.01.0500	Tb927.11.8040	Q384L5	185	104-185	
<b>mL89</b>	BW	Tb427.03.820	Tb927.3.820	Q57WW5	188	2-188	
<b>mL90</b>	BX	Tb427.06.1700	Tb927.6.1700	Q585P1	190	61-100, 108-174	2x Zn binding
<b>mL92</b>	BZ	Tb427tmp.01.1215	Tb927.11.9450	Q383Y4	190	2-190	
<b>mL93</b>	Ba	Tb427.10.11350	Tb927.10.11350	Q389K5	153	19-153	
<b>mL94</b>	Bb	Tb427tmp.160.5050	Tb927.9.6910	Q38EP7	162	38-140	
<b>mL95</b>	Bc	Tb427.10.11370	Tb927.10.11370	Q389K3	146	10-146	
<b>mL98</b>	Bf	Tb427.10.13770	Tb927.10.13770	Q388M2	113	27-68, 75-112	
<b>mL99</b>	Bg	Tb427.02.2590	Tb927.2.2590	Q587H8	105	24-105	
<b>mL100</b>	Bh	N/A	Tb927.9.8905	N/A	92	2-91	Zn binding
<b>mL101</b>	XR	Tb427.01.1390	Tb927.1.1390	Q4GZ80	245	22-203	
<b>mt-ACP1</b>	XD	Tb427.03.860	Tb927.3.860	Q57WW9	148	64-146	
<b>mt-ACP2</b>	XE	Tb427.03.860	Tb927.3.860	Q57WW9	148	64-146	
<b>mt-EngA</b>	XL	Tb427.07.1640	Tb927.7.1640	Q57TZ4	576	45-504, 514-574	2xGTP binding
<b>GTPBP7</b>	XQ	Tb427tmp.211.0810	Tb927.9.9150	Q38E75	451	44-202,215-338	
<b>L0R8F8</b>	XM	Tb427.07.4210	Tb927.7.4210	Q57UQ1	116	25-115	
<b>MALSU1</b>	XJ	Tb427.06.3420	Tb927.6.3420	Q584Y2	349	163-312	
<b>MRM</b>	XO	Tb427tmp.211.3800	Tb927.9.12850	Q38DC9	586	78-344, 363-440, 453-505	
<b>RPUSD4</b>	XP	Tb427tmp.160.2000	Tb927.9.3350	Q38FJ3	406	35-405	
<b>mt-LAF2</b>	XB	Tb427tmp.52.0011	Tb927.11.12930	N/A	754	47-391, 443-711	MgADP binding
<b>mt-LAF4</b>	XC	Tb427tmp.02.3800	Tb927.11.5990	Q385G9	616	1-414, 444-616	
<b>mt-LAF7</b>	XA	Tb427.10.15860	Tb927.10.15860	Q387S8	156	3-156	Zn binding

<b>mt-LAF8</b>	XH	Tb427.05.2070	Tb927.5.2070	Q57ZS6	634	2-55, 86-113, 184-276, 300-336, 367-412, 471-577, 587-623	
<b>mt-LAF12</b>	XN	Tb427.08.3300	Tb927.8.3300	Q57YY3	691	58-101, 123-150, 200-668	
<b>mt-LAF14</b>	XI	Tb427.05.3870	Tb927.5.3870	Q57U79	731	25-95, 156-203, 213-289, 319-647, 656-727	
<b>mt-LAF15_1</b>	XF	Tb427.04.4610	Tb927.4.4610	Q583E6	319	120-170, 194-245, 260-317	
<b>mt-LAF15_2</b>	UF	Tb427.04.4610	Tb927.4.4610	Q583E6	319	1-34, 37-87, 92-105, 122-135, 140-167	built as UNK
<b>mt-LAF18</b>	XR	Tb427tmp.211.4580	Tb927.9.14050	Q38D50	524	2-165	
<b>mt-LAF19</b>	XS	Tb427tmp.01.1810	Tb927.11.10050	Q383S4	102	6-102	

**Table S3. Contacts of assembly factors with rRNA.** Regions and nucleotides of respective rRNA domains corresponding Fig EV4 and Appendix Fig S6.

Assembly factor	Contacts with rRNA	
	Region	Nucleotides
mt-EngA	H74, H75, H88, H90-91	868-874, 891-898, 958-967, 986-989
GTPBP7	H90-91	1013, 1071
MALSU1	H95	1126-1132, 1138-1141
MRM	H43, H90, H95	409-413, 1012-1013, 1136-1137
RPUSD4	H39, H90-93	351-353, 857-859, 984-986, 1003, 1005-1013, 1071-1087, 1122-1124
mt-LAF2	H26, H32, H33, H35a, H37, H39, H51, H72, H73-75, H80-81, H93	127-139, 199-200, 270-276, 289-293, 306-316, 344-355, 497, 550, 555, 826-828, 847-848, 850-855, 860-862, 870, 903-922, 930-933, 947-950, 955-965, 975 -984, 1085-1089
mt-LAF4	H13, H28, H37, H80-81, H88	65-66, 164-166, 313, 328, 908, 917-919, 935-939, 944-953
mt-LAF7	H39, H43, H72, H74, H88, H93	132-135 347-351, 404, 821-829, 832-835, 860-862, 904, 965-677, 977-984, 1079-1082, 1119
mt-LAF8	H41, H43	407, 448-450
mt-LAF12	H95	1131-1140
mt-LAF14	H80-81, H88	908-909, 915-916, 919-924, 930-940, 952-957, 961
mt-LAF15	H43	411-412, 446